Remote Sensing of Environment 258 (2021) 112400

Contents lists available at ScienceDirect

Remote Sensing of Environment

journal homepage: www.elsevier.com/locate/rse

InSAR monitoring of creeping landslides in mountainous regions: A case study in Eldorado National Forest, California

Ya Kang [a,b], Zhong Lu [b,*], Chaoying Zhao [a], Yuankun Xu [b], Jin-woo Kim [b], Alan J. Gallegos [c]

[a] School of Geology Engineering and Geomatics, Chang'an University, Xi'an 710054, China
[b] Roy M. Huffington Department of Earth Sciences, Southern Methodist University, Dallas, TX 75275, USA
[c] US Forest Service, PSW Region 5, 1600 Tollhouse Road, Clovis, CA 93611, USA

ARTICLE INFO

Editor name: Jing M. Chen

Keywords:
InSAR
Segment processing
Landslide
Eldorado national forest
Geohazard

ABSTRACT

Monitoring surface deformation associated with geohazards is a prerequisite for geological disaster prevention. Interferometric synthetic aperture radar (InSAR) has the ability to capture ground deformation of landslides with high precision over a large area. However, in mountainous regions this capability is often limited by decorrelation noise and atmospheric phase artifacts. Over Eldorado National Forest, California, where many landslides need to be monitored and investigated, InSAR images are severely affected by atmospheric noise and the coherence is highly variable throughout the year, challenging InSAR techniques to effectively detect movement of active landslides. In order to obtain reliable measurements, we have designed an interferogram selection method and an InSAR segment processing (SP) technique to improve the deformation measurement. Compared with the traditional non-segment processing (NSP), the SP technique has demonstrated advantages in reducing the impact of atmospheric noise. Our results from both the ascending and descending InSAR datasets based on SP indicate that many landslides along the Highway 50 corridor were creeping at a rate of less than 10 cm/year during the investigation period. We have found that landslide movements in the study region present obvious seasonal patterns. The precipitation and pore-water measurements and our hydrogeological diffusion models suggest that the seasonal movements of these landslides are primarily driven by the pore-water pressures, and the peak deformation of the landslides may occur in the dry season (May to October) due to the time lag of precipitation infiltration. In addition, we have observed subtle upward movement of the landslides after the precipitation begins, which is likely caused by the swelling of clay-rich landslide body due to an increase in the pore pressure. Furthermore, several other localized unstable regions which may contain potential landslide hazards were also detected and mapped in the study area, and their dynamics need further investigation. We conclude that InSAR is capable of detecting slow landslide motions over difficult terrains if associated artifacts in the interferograms are suppressed. InSAR time-series measurements along with hydrogeological models enable us to characterize the time delay between peaks of landslide motions and precipitation.

1. Introduction

In recent years, InSAR has been widely used to map geohazards of various scales, such as landslides (e.g. Hu et al., 2016; Hu et al., 2019; Handwerger et al., 2019), sinkholes (e.g. Kim et al., 2019) and anthropogenic activities (e.g. Kim and Lu, 2018; Zheng et al., 2019). For these geohazards, InSAR measurements could be used to provide key information to understand the mechanism of movement (e.g. Kang et al., 2019; Zheng et al., 2019; Liu et al., 2020), and can also be used to invert physical parameters (e.g. Hu et al., 2019; Hu and Bürgmann, 2020; Nikolaeva et al., 2014). For many geohazards (such as a single landslide), researchers only need to focus on localized deformations in small areas (e.g. Hu et al., 2016; Kang et al., 2019), in which the long-wavelength error has limited impact on the InSAR measurement (e.g. Parizzi et al., 2020). However, when the scale of the study area becomes larger, errors of various length scales should be considered and corrected. When the mapping is performed in a rural region with huge elevation variations, due to the impact from the decorrelation and atmospheric noise (especially the topography-correlated component), the errors are more difficult to correct. Therefore, it is of great importance for InSAR studies to effectively separate the deformation from errors in data processing. At present, although many methods have been

* Corresponding author.
E-mail address: zhonglu@smu.edu (Z. Lu).

https://doi.org/10.1016/j.rse.2021.112400
Received 26 October 2020; Received in revised form 11 February 2021; Accepted 13 March 2021

proposed to correct various errors, they should be selected and used according to the actual situation in complex environments (e.g. Biggs et al., 2007; Liang et al., 2018).

The study area, encompassing several water bodies and two highways, is located within the Eldorado National Forest, in central California (Fig. 1). The topography in this area varies by 2611 m with higher elevations in the east side and lower elevations on the west side of the block. As shown in the Fig. 1(b), the maximum and minimum elevations of the study area are 3147 m and 536 m above mean sea level, respectively. Average monthly weather data of the Pacific House weather station (the location of this station is shown in the Fig. 1) were collected at and accessed from the Western Regional Climate Center (https://wrcc.dri.edu/). Based on the record from 1941 to 2016, February has the lowest average monthly temperature (−2.2 °C), and August has the highest average monthly temperature (33.3 °C) (see Supplementary Fig. S1). Precipitation mainly occurs in winter and spring, and the average monthly precipitation peaks in January. The cold winter storms may bring snow (Reid et al., 2003). Based on the data from the National Integrated Drought Information System (NIDIS) (https://www.drought.gov/drought/), from 2000 to 2020, the longest duration of drought (moderate to exceptional drought) in El Dorado County lasted 194 weeks beginning on April 23, 2013 and ending on January 3, 2017.

The area surrounding Highway 50 is a landslide-prone region (Fig. 1), with more than 600 landslides mapped along the 24 km-long highway corridor (Spittler and Wagner, 1998), and there have been several large-scale landslides and runout events that caused temporary closures of the highway, the most significant of which occurred in 1997 (Spittler and Wagner, 1998). These landslides are located at the steep slopes of the canyon carved by the South Fork of the American River. Along the corridor, there are large amounts of deeply weathered materials, such as weathered quartz-mica schist and granitic material, which have produced a deep layer of colluvium (Berube, 1999). When the deposit along the corridor is comprised by the colluvium or weathered materials, it becomes unstable under proper conditions (Berube, 1999; Spittler and Wagner, 1998). In the west region of Twentynine Mile Guard Station (the location of this guard station is shown in the Fig. 1), the deposits usually contain a thick oxidized soil horizon (Spittler and Wagner, 1998). In this region, some landslides have been monitored, such as the Cleveland Corral landslide (Reid and Brien, 2019; Aryal et al., 2012; Reid et al., 2003), since 1997. The Cleveland Corral landslide is active in winter and spring of wet years. The material of the main slide consists of colluvium and older landslide deposits and are composed of cobble-sized of schist (10–15%), sand (27–61%), silt (18–47%), and clay (14–33%) (Reid et al., 2003). And, some parts of the

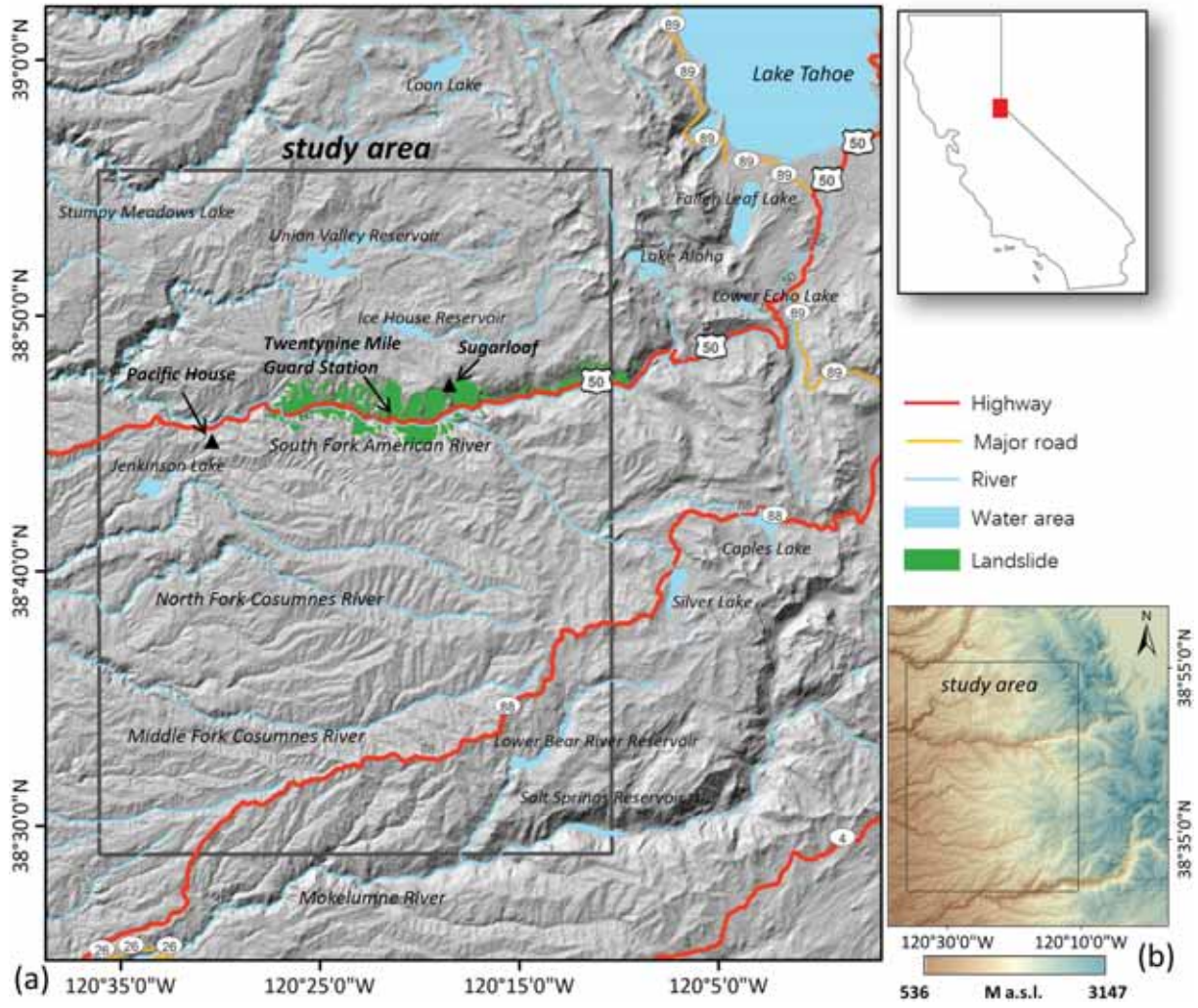

Fig. 1. (a) The location and topography of the study area. The study area is located in the Eldorado National Forest, in northern California. The gray rectangle shows the range of the study area. The black triangle represents the locations of the Pacific House and the Sugarloaf weather station. The landslide coverage depicted in green was acquired from the California Geological Survey (CGS) (https://gis.conservation.ca.gov/server/rest/services); (b) The digital elevation model of the study area. (For interpretation of the references to colour in this figure legend, the reader is referred to the web version of this article.)

sliding material are clay rich (Reid et al., 2003).

Monitoring landslide deformation can help us better understand the mass propagation in space, motion evolution in time, and the driving factors (Hu et al., 2019). However, the spatial-temporal characteristics of the creeping stage deformation for many of these landslides along Highway 50 have not yet been determined. In addition, we do not know the movements of many other unstable areas in the study region due to the limited effort to capture those through remote sensing techniques or in-situ observations. Therefore, in order to further understand the development of potential disasters in this region, it is necessary to detect, monitor and analyze these unstable regions. InSAR, as a powerful remote sensing technology with a high-resolution and large area coverage, was applied to map and characterize the local creeping deformation for the study area.

In this paper, we begin by analyzing the coherence of all the interferograms. Since the interferograms could not keep enough coherence in winter and early spring, a new interferogram selection method based on coherence is used to select the interferograms. Then, considering the huge elevation variations of the study area, an InSAR processing method based on local estimation windows is designed to map the local unstable regions. This has enabled the recovery of the creeping deformation of the landslides along Highway 50. The cause of the landslides' seasonal deformation is discussed and analyzed with the precipitation and pore-water pressure modeling. We finally present new insights to the behaviors of the landslides along Highway 50 corridor.

2. Data and Interferograms selection

Sentinel-1 A/B data were used to image the deformation. Two polar-orbiting satellites (Sentinel-1A and Sentinel-1B) constitutes the Sentinel-1 mission, which were launched by the European Space Agency (ESA) in 2014 and 2016, respectively. These two satellites have the same orbital plane, which allows a 6-day revisit period of the constellation. In this study, 119 Sentinel-1 A/B ascending track images and 108 Sentinel-1 A/B descending track images were collected. The time span for ascending track data was from January 2016 to September 2019, and from March 2015 to September 2019 for descending track data. Due to the availability of the archived Sentinel-1A/B data over this area, the time spans of these two datasets are different. Since the results from these two datasets were processed and inverted individually, this inconsistency will not affect the results and interpretation of the time series deformation. Time span inconsistency may have some influence on estimating the linear deformation rates. However, the common time span of these two datasets accounts for the main part of the monitoring period (i.e., Jan 2016 - Sept 2019). Hence, the inconsistency on the start times of the datasets in our case has little effect on the linear deformation rate. In addition, the linear deformation rate is only used to map/show the unstable areas in this study. Therefore, the inconsistency of the time spans has little impact on the interpretation. The 1-arc-second SRTM DEM was used to remove the topographic phase, geocode the results and segment the interferograms, and the precise orbit data were collected and used in the processing. The threshold of the temporal and spatial baselines was set to 90 days and 200 m, respectively. Then, 1098 interferograms in the ascending track and 611 interferograms in the descending track can be obtained (the configurations of the baseline are shown in Supplementary Fig. S2 and S3). The interferograms were routinely processed and acquired by GAMMA software (Werner et al., 2000). The satellite-derived precipitation can be useful in landslide analysis (e.g. Hong et al., 2006). The Global Precipitation Measurement (GPM) used in this study provides precipitation estimates at spatial resolutions of 0.1°x0.1° and temporal resolution of 1 day (Huffman et al., 2019). The GPM covering the whole study area was collected and used to explore the relationship between the seasonal precipitation of the study area and the coherence of the interferograms. Compared to the single weather station, the GPM can reflect the precipitation changes of the whole study area more comprehensively. In addition, the daily precipitation of the Pacific House and the Sugarloaf weather station were collected from the National Oceanic and Atmospheric Administration (https://www.noaa.gov/) and the Western Regional Climate Center (https://wrcc.dri.edu/) respectively. The locations of these two weather stations are shown in Fig. 1.

Located in El Dorado National Forest, our study area is covered by dense vegetation, which causes most interferogram pixels to decorrelate substantially with time (e.g. Lu et al., 2002; Hooper et al., 2007). In addition, compared with the L-band data, the C-band Sentinel-1 interferograms are more easily to lose coherence due to the short wavelength (Zebker and Villasenor, 1992). The average coherence is generally much lower in winter and spring than in summer, due to precipitation (Fig. 2). In the rainy season, the coherence for many interferograms was too poor to acquire reliable monitoring points. This is especially problematic for landslide identification and monitoring, where dense monitoring points are often needed. Furthermore, the low coherence region may cause unwrapping errors, which will further worsen the monitoring accuracy (Lauknes et al., 2010).

In order to obtain reliable results, high quality interferograms can be selected manually (Lee et al., 2010; Zhao et al., 2012; Lu and Dzurisin, 2014; Kang et al., 2019). However, with a large amount of SAR data, manual selection requires a costly labor investment. We therefore propose a concept of Effective Coherence Ratio (ECR) used to select the interferograms in this study. The ECR is defined as the ratio of the area with coherence higher than a threshold to the whole image area. We assume that when the coherence of a region is lower than this threshold, it is almost impossible to extract reliable signal from this region. The coherence of regions covered by water was set as the threshold to estimate the ECR in this study. Repeat-pass InSAR cannot reliably acquire deformation signals from water regions without other reflectors (e.g., Lu and Kwoun, 2008). Since the calm water surface has the characteristics of specular reflection, the theoretical coherence over calm water is zero. However, completely calm water regions may not exist in nature due to wind, tides, and human activities. In addition, the coherence estimation is biased. Therefore, the coherence is generally not zero in the water. We averaged the coherence maps of all the interferograms, and found the average coherence of the water regions to be about 0.15. In this study, the threshold of coherence was set as 0.15, and the interferograms with ECR higher than 75% were selected for further processing. The configurations of the selected interferograms based on ECR are shown in Supplementary Fig. S2 (b) and S3 (b).

The interferograms selected by ECR were used to invert the time-series deformation. However, we found that more than half of the selected interferograms from the ascending track were from the year 2018. When the stacking method is used to invert the linear deformation

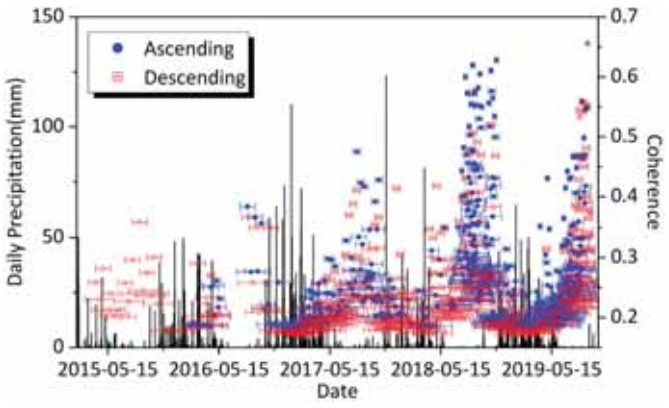

Fig. 2. The average coherence of the interferograms. The horizontal bars represent the time span of the interferograms. The black lines represent the average daily precipitation of the study area, which is collected from the Global Precipitation Measurement (GPM) (Huffman et al., 2019).

rate, the estimated result will be closer to the deformation rate of 2018. In order to avoid the bias of large concentration of data from one time period, the non-redundant interferograms were selected through the minimum spanning tree (MST) algorithm (Kruskal, 1956) and then used for the linear deformation inversion. The configurations of the non-redundant interferograms are shown in Supplementary Fig. S2 (c) and S3 (c).

3. Segment processing

In many studies, the accuracy of InSAR is severely limited by atmospheric noise (Bekaert et al., 2015b; Murray et al., 2019). Separating the deformation and the atmospheric signal is challenging work (Hooper et al., 2012; Bekaert et al., 2015b; Murray et al., 2019). The impact from atmospheric noise on the interferograms can be evaluated by using structure function in Eq. 1 (Lohman and Simons, 2005; Murray et al., 2019).

$$\delta(k) = E\left[(\varphi(x) - \varphi(x+k))^2\right] \quad (1)$$

In which $\varphi(x)$ is the unwrapped phase at position x, $\delta(k)$ is the variance with a distance k. Although, only the impact factor of the distance k for the spatial noise is considered, the structure function has some useful characteristics. This function has been used to describe the spatial structure of the atmospheric noise in many previous studies (Lohman and Simons, 2005; Murray et al., 2019; Cao et al., 2018). The spatially correlated noise is evaluated by the structure function, and the characteristics of the distance related variance for the selected interferograms are shown in Fig. 3.

For the original unwrapped interferograms, the variance of two points was found to increase continuously with the increase in distance between these two points. This indicates that the interferograms are affected by the long-wavelength signal in the study area. Considering the

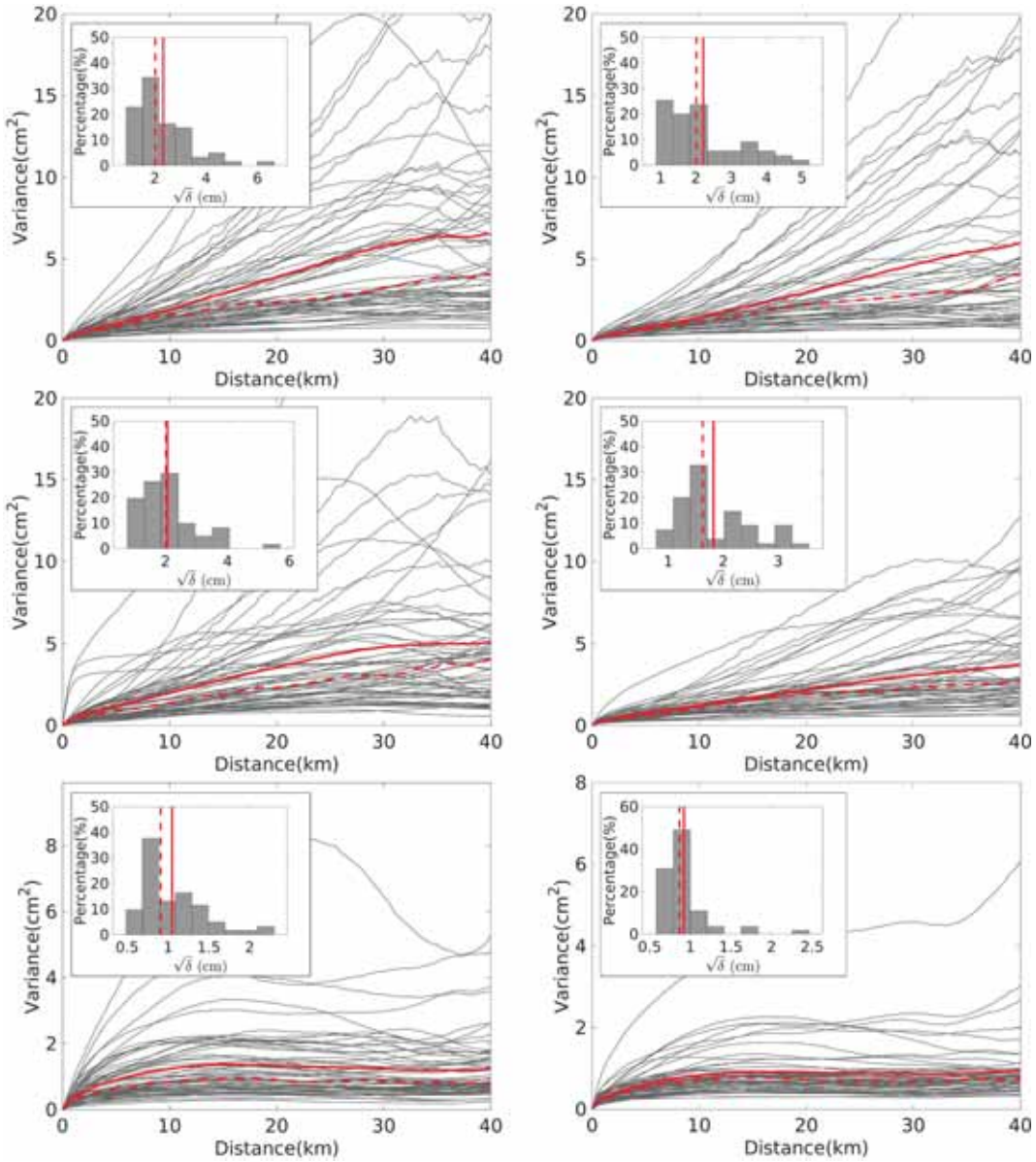

Fig. 3. The variance versus distance for the interferograms. The red solid and dash lines show parametrized 1-D structure function with the average and median values respectively. Insets show distribution of the standard deviation ($\sqrt{\delta}$) between the two points at distance of 40 km. (Left) Interferograms from ascending dataset; (Right) Interferograms from descending dataset; (Top) Original Interferograms; (Middle) Interferograms corrected by Generic Atmospheric Correction Online Service for InSAR (GACOS); (Bottom) Interferograms corrected by removing the phase ramp and topography related tropospheric delay. (For interpretation of the references to colour in this figure legend, the reader is referred to the web version of this article.)

trend of terrain in the study area, we suggest that the atmospheric noise is a major contributor to the characteristics of the long-wavelength signal. Since many previous studies have shown that the Generic Atmospheric Correction Online Service for InSAR (GACOS) performs well on atmospheric delay correction (Murray et al., 2019; Albino et al., 2019; Yu et al., 2018), we collected the GACOS data and used it to remove the atmospheric phase screen (APS) of the interferograms. We found that the spatially correlated signal of the interferograms can be reduced by the GACOS to a certain extent (Fig. 3, middle row). Finally, the phase-based atmospheric corrections were also tested against the original interferograms (Fig. 3, bottom row). The topography related tropospheric delay were first corrected by a linear phased-based model (Murray et al., 2019). And then, considering the long spatial-scale tropospheric component (Murray et al., 2019), a quadratic model was used to separate the phase ramp (Wang et al., 2012). It can be found that, for many interferograms, the distance related variances of the interferograms corrected by the phase-based methods are smaller than the variance by the GACOS. It should be noted that the long-wavelength non-atmospheric signal can also be filtered out by the phase-based model. We need to be cautious in using polynomials to fit the atmospheric noise over areas possessing a long-wavelength deformation signal. Since only the local deformations are focused by this study, the phase-based corrections are used in the data processing.

After the phase-based correction, the variance stops increasing once the distance reaches a certain value. For the phase-based corrected interferograms, the average standard deviations from both the ascending and descending datasets reached about 1 cm when the distance exceeded 20 km. Therefore, although these phase-based corrected interferograms were used to invert the deformation, the residual atmospheric noise may have the same magnitude as the deformation of the creeping stage landslides in regions far away from the reference point.

The tropospheric delay can be divided into three components: the topography correlated delay (or the vertically stratified component), the long spatial-scale component and the turbulent mixing component (Murray et al., 2019). The interferograms are often strongly affected by the vertically stratified component in the regions with high relief (Murray et al., 2019). The linear or the power-law model can be used to estimate the vertically stratified component (Bekaert et al., 2015a; Bekaert et al., 2015b; Wang et al., 2012). However, over large spatial scale and/or huge elevation variations, it is very difficult to use these models with fixed parameters to accurately estimate the vertically stratified component for the whole image (Bekaert et al., 2015a; Liang et al., 2018). This is because the relationship between the vertically stratified component and the topography varies spatially, and this relationship cannot be simply regarded as linear or power law in the case of huge elevation variations (Bekaert et al., 2015a; Liang et al., 2018). To solve this problem, some local-window based methods have been proposed (e.g. Liang et al., 2018; Bekaert et al., 2015a; Béjar-Pizarro et al., 2013). The vertically stratified component can be estimated more accurately based on small local windows (Liang et al., 2018). In addition, due to some long wavelength errors (especially the atmospheric noise), the phase variance of two points increases with the distance between these two points (Murray et al., 2019; Biggs et al., 2007). This phenomenon can also be found in Fig. 3. So, the monitoring accuracy of the points closer to the reference point are often higher than that of points further away from the reference point (Cao et al., 2018).

Considering the huge elevation variations of the study area and error accumulation in spatial domain, a segment processing (SP) method was designed for use in this study. First, in order to estimate the vertically stratified tropospheric delay accurately, an interferograms segmentation method based on quadtree was applied (Liang et al., 2018). Then, the vertically stratified tropospheric component was corrected for each segment individually. Next, in order to restrain the error accumulation in spatial domain, both the reference point selection and deformation inversion were performed within each segment directly. And finally, the results for the segments were merged to form a single deformation map. It should be noted that this study only focuses on localized deformation. This SP method is not suitable for long-wavelength deformation, such as faulting and large-scale ground subsidence.

3.1. Quadtree segmentation

In this study, all interferograms were divided into small segments according to the height difference by quadtree (Liang et al., 2018). This means that the window was divided into 4 small windows if the maximum height difference in this window was larger than a threshold. In addition, once the window size reached the minimum threshold, the window would not be further divided. There is a 25% overlap between adjacent windows. More details about the window segmentation can be found in Liang et al. (2018).

The threshold of height difference was set at 1000 m. Since the deformation is inverted in each segment separately in this study, the minimum window size depends on the scale of the monitoring target. Since the focus of this study was only on small-scale landslides, the minimum window size was set at 10 km across. The schematic diagram of the quadtree segmentation is shown in Fig. 4.

3.2. Tropospheric delay correction and deformation inversion

After the segmentation, the vertically stratified component and the phase ramp can be estimated simultaneously by a quadratic model for each segment in Eq. 2 (Xu et al., 2013; Kang et al., 2017).

$$\mu(x,y) = b_0 + b_1x + b_2y + b_3xy + b_4x^2 + b_5y^2 + b_6\eta(x,y) \quad (2)$$

where μ denotes the vertically stratified component and the long spatial-scale component of the tropospheric delay, η is the elevation, b_i represents unknown coefficients. The deformation would cause biases into the phase-based tropospheric delay correction (Dong et al., 2019). Therefore, the processing flow of the tropospheric delay correction and deformation inversion for each segment was designed as follows.

Step 1: the tropospheric delay is estimated and separated based on the Eq. (2). The observations with a low coherence are masked to reduce the influence from decorrelation noise in the phase-based tropospheric delay estimation.

Step 2: the preliminary linear deformation rate is inverted through stacking-InSAR based on the corrected observations from the previous step 1. Then, the preliminary unstable points and the reference point for each segment can be determined based on the linear deformation rate and its standard deviation.

Step 3: the tropospheric delay is re-estimated and separated based on the Eq. (2) for the original unwrapped phase, and the identified preliminary unstable regions are masked during this tropospheric delay estimation.

Step 4: the linear and time-series deformation rate are inverted based on the refined unwrapped phase from step 3 and the selected reference point from step 2.

The detailed processing of the reference point selection and the deformation inversion for each segment is described further in Sections 3.2.1 and 3.2.2.

3.2.1. Reference point and preliminary unstable points

The reference phase is critical for the deformation inversion and mechanism explanation. However, inverting the deformation by setting a single reference point (or the average phase around it) might be unreliable (e.g. Finnegan et al., 2008; Wang et al., 2012). For the preliminary linear deformation rate inversion, the reference phase was set as the average phase of the whole segment (Finnegan et al., 2008; Wang et al., 2012). This is reasonable here because the focus is only on local deformation, rather than the large-scale deformation (Wang et al., 2012). After the preliminary linear deformation rate and its standard deviation are acquired, we assume that the unstable region does not

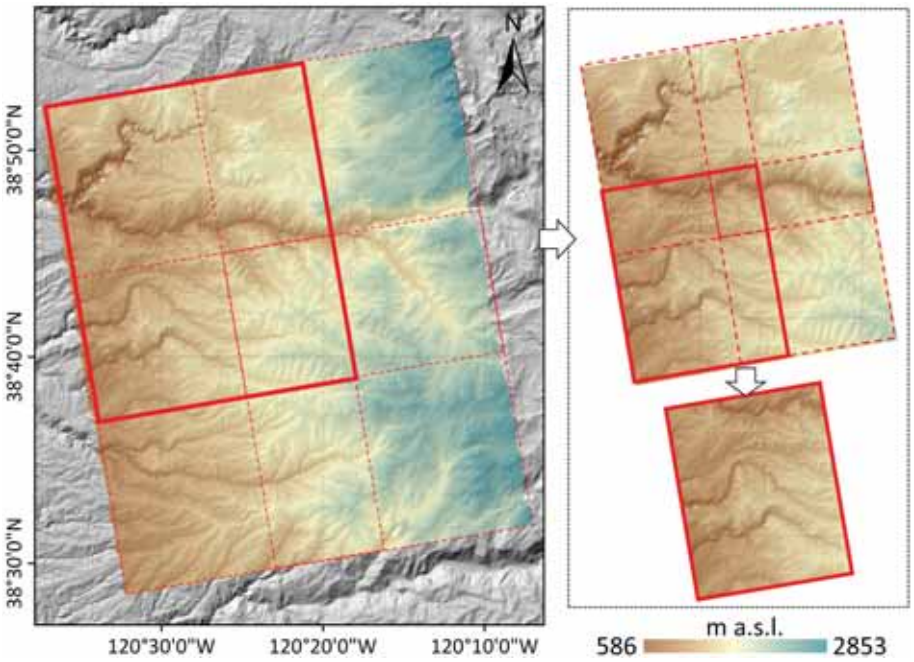

Fig. 4. The schematic diagram of quadtree segmentation. If the maximum height difference within a window exceeds the threshold (1000 m in this study), this window will be divided into four small windows. Red rectangles represent the windows. The adjacent windows have an overlap of 25% window size. (For interpretation of the references to colour in this figure legend, the reader is referred to the web version of this article.)

exceed 50% of the segment. So, 50% of the pixels with relative larger deformation are set as the preliminary *unstable* points that will be masked during the second-time tropospheric delay estimation based on Eq. (2). The other 50% of pixels are set as the preliminary *stable* points in the following reference point selection. In the same scene, the standard deviation of the linear deformation rate of the unstable regions may be larger than that of the stable regions because the deformation may include the linear and nonlinear deformation component. In addition to noise, the nonlinear deformation component can also increase the standard deviation of the linear deformation rate. So, in order to further reduce the influence of the deformation on the reference phase, the preliminary *stable* points with relative lower standard deviations are selected as the reference points. Then, the average phase of a selected reference points is set as the reference phase for the final deformation inversion for each segment. In this study, 5% of the preliminary *stable* points with relative lower standard deviations were selected as the reference points.

3.2.2. Deformation inversion

The Stacking-InSAR method is used for linear deformation rate inversion (e.g., Kwoun et al., 2006; Wang et al., 2012). In order to further reduce the decorrelation noise, only the observations with a coherence higher than a certain threshold (0.45 in this study) were used to invert the linear deformation rate for each segment. The linear deformation rate and DEM errors were estimated simultaneously, and then the DEM errors were corrected in each interferogram for the following time-series deformation inversion.

The Intermittent Small Baseline Subset (ISBAS) was used to invert time-series deformation (Sowter et al., 2013). Unlike the traditional Small Baseline Subset (SBAS) technique (Berardino et al., 2002), pixels that are coherent only for parts of the stack of interferograms can also be processed in ISBAS (Sowter et al., 2013). Therefore, the monitoring points obtained by ISBAS is usually denser than that obtained by SBAS (Sowter et al., 2013; Bateson et al., 2015; Cigna and Sowter, 2017). In addition, the reliability of ISBAS measurements has been validated in many applications (Sowter et al., 2016; Gee et al., 2016; Novellino et al., 2017; Gee et al., 2020). In this study, in order to increase the available monitoring points, for one location (one pixel), all the observations (unwrapped interferogram phases) with a coherence higher than a certain threshold were used to invert the time-series deformation rate between the adjacent SAR data (Supplementary Fig. S4). The coherence was used as the weight in the inversion to reduce the decorrelation noise. The interferograms were separated into several subsets, with no overlap between the subsets. Therefore, the cumulative time-series deformation could not be recovered, but only the time-series deformation rates during the coherent periods were inverted and analyzed.

3.3. Merging of results from segments

After the deformation inversion, the results from each segment can be merged. The result in the overlapping areas are set as the average value from the different segments. Then, the minimum standard deviation of the linear deformation rate for the water region was set as a threshold to mask the unreliable linear deformation rate. It should be noted that the turbulent mixing component cannot be corrected based on the Eq. (2). The turbulent mixing component is generally considered to be temporally random (Ferretti et al., 2001; Wang et al., 2012). So, for the linear deformation rate, the turbulent mixing component can be effectively reduced by Stacking-InSAR. However, the turbulent mixing component still has a significant impact on the time-series deformation, without further processing. Because the atmospheric noise occurs on each SAR image, the turbulent mixing component cannot be separated through SVD or the L-2 norm for the time-series deformation. The turbulent mixing components are spatially correlated and temporally random (Ferretti et al., 2001). At last, the turbulent mixing component was separated from the time-series deformation through use of a temporal high-pass filter and a spatial low-pass filter (one- and two-dimensional Gaussian kernel in time and space, respectively) (Wang et al., 2012; Morishita et al., 2020). The window size for the temporal filter was set at 36 days, which is about three times the average temporal sampling interval (Morishita et al., 2020). And the spatial filter window size was set at 10 km, which is the minimum segment size. The flow chart for the SP method is shown in Fig. 5.

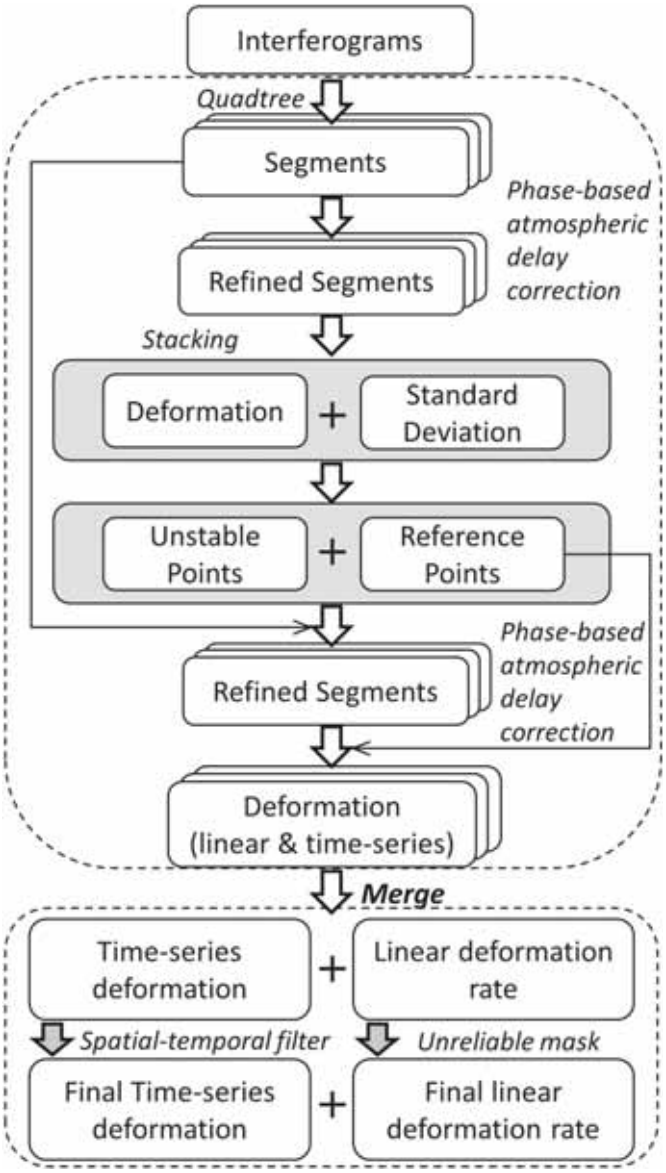

Fig. 5. The flow chart of the InSAR Segment Processing (SP).

4. Evaluation of InSAR segment processing

In order to evaluate the performance of the SP, three additional processing strategies were also tested for comparison. The first one is called non-segment processing (NSP), in which the phase-based methods are used to correct the tropospheric delay. The whole interferogram is used to fit the topography related tropospheric delay and the phase ramp based on a linear phased-based model and a quadratic model respectively (Wang et al., 2012). A stable point with high coherence is manually selected as the reference point for the whole image. The deformation inversion of NSP is the same as the SP. Lastly, the residual atmospheric delay from NSP are separated from the time-series deformation by a spatial-temporal filter. The interferograms and the parameters used in the NSP are consistent with that used in the SP. The second alternative strategy is called the non-segment processing with the GACOS correction (NSPG). NSPG differs from NSP in that we didn't use phase-based methods to correct the interferograms, but instead corrected the atmospheric delay by GACOS. The third alternative method to SP is called non-segment processing within a local estimation window (NSPW). The only difference between NSPW and NSP is that we estimate the topography-related tropospheric delay and the phase ramp within a local window.

5. Results and discussion

5.1. Deformation rate and precision analysis

Based on the selected interferograms, the linear deformation rates from the ascending and descending tracks can be obtained through SP, NSP, NSPG and NSPW separately. The resulting linear deformation rates using SP, NSPG and NSP are shown in the left columns, middle columns and right columns of Figs. 6 and 7 respectively. In addition, the linear deformation rate and the standard deviation from the NSPW and the local estimation window are shown in the Supplementary Fig. S5.

The standard deviation can reflect the inner precision of the linear deformation rate. Because many factors can increase the standard deviation of linear deformation rate, such as the nonlinear deformation, decorrelation noise and atmospheric noise, the standard deviation is only used for relative comparison in each dataset. In addition, the standard deviation can also be used to evaluate the uncertainty of the measurements. It can be seen that both the standard deviation of NSP and NSPG are relatively larger in the areas further away from the reference point, particularly over the valleys with significant topographic relief. The linear deformation rates from both NSP and NSPG still have an obvious correlation with the topography in some regions. For example, for certain valleys, the positive deformation always appears (as shown in Figs. 6 and 7, middle and right columns). These phenomena show that it is difficult to accurately estimate the topography-related atmospheric delay using a phase-based correction with a fixed parameter in a region with large elevation variations, and the GACOS products are unable to completely remove the topography related atmospheric delay in this study area. In addition, the precision of the results is relatively lower with increasing distance from the reference point. For the results from the NSPW, we found that the standard deviation is relatively small in the local estimation window compared with results from the NSP and NSPG (the results form NSPW are shown in the Supplementary Fig. S5). This indicates that the phase-based atmospheric correction is more suitable for a local region, rather than for the whole image. Furthermore, in the landslide-rich region along Highway 50, the magnitude and scale of the linear deformation rate obtained by NSPW and SP are consistent in the local estimation window. This further confirms the reliability of the results obtained by SP.

We found that the mean standard deviation obtained based on NSP (1.3 cm/year ascending and 1.4 cm/year descending) is generally smaller than that based on NSPG (2.6 cm/year ascending and 2 cm/year descending) in this study. This is because GACOS is obtained from 6-hourly High Resolution ($0.125^\circ \times 0.125^\circ$ horizontal resolution) European Centre for Medium-Range Weather Forecasts (ECMWF) and GPS data (Yu et al., 2018). The effect of GACOS is highly dependent on the distribution of the GPS station, SAR acquisition time and the location of the study area. Therefore, the corrective capability of GACOS differs by region. In addition, some long-wavelength non-atmospheric signals can also be fitted by polynomials. It can be seen that the GACOS based NSPG method is not suitable for this study. So, in the following analysis, we mainly compare the results of SP and NSP.

As shown in the Figs. 6 and 7, the standard deviation from SP (mean of 0.84 cm/year ascending and 1 cm/year descending) is generally lower than that from NSP (mean of 1.3 cm/year ascending and 1.4 cm/year descending). That is, SP improves the average inner precision of the linear deformation rate by about 30% over NSP. It also can be found that the standard deviations of the results in this study are much higher than that in some other studies (e.g. Wang et al., 2012; Cigna and Sowter, 2017). The larger standard deviations are caused by the environment characteristics of the study area: interferograms are severely affected by atmospheric artifacts and decorrelation noise.

The minimum standard deviation in the water area is set as the threshold to mask the unreliable results (Supplementary Fig. S6). The

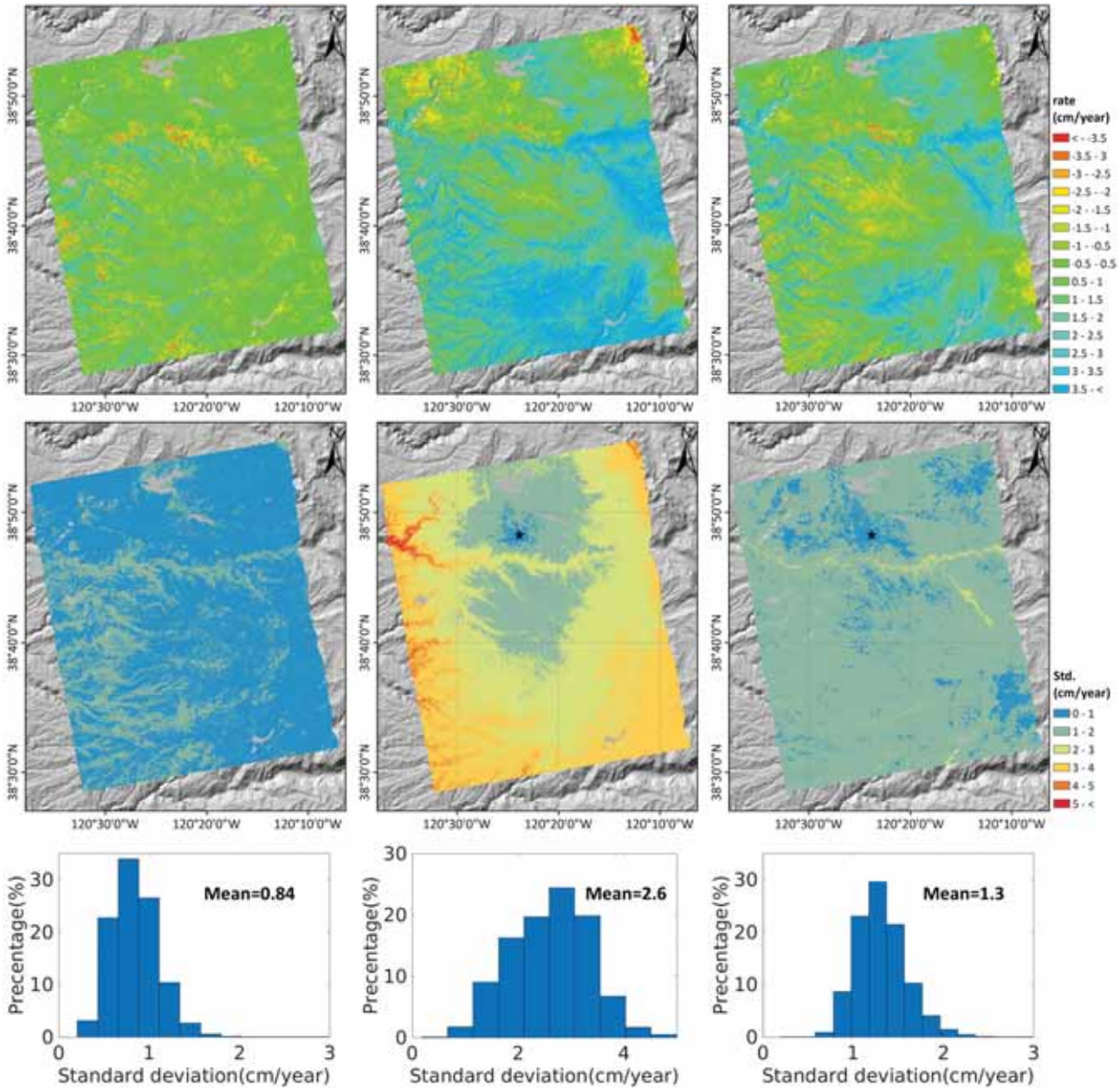

Fig. 6. A comparison of ascending dataset results for linear deformation rate (top row), standard deviation of the deformation rate (second row) and histogram of the standard deviation (bottom row) for three processing methodologies: SP, NSPG, and NSP. The left column shows segment processing (SP) results; the center column shows non-segment processing with the GACOS correction (NSPG) results; the right column shows non-segment processing (NSP) results. The black star represents the reference point used for NSPG and NSP.

final linear deformation rates from SP are shown in Fig. 8. It should be noted that since the interferograms in winter and early spring are seldom selected, the linear deformation rate of the unstable regions may be biased.

Fig. 9 compares the histograms of the linear deformation rate difference in the overlap area between the two different (ascending and descending) tracks for both SP and NSP. In some unstable regions, especially for landslides with significant horizontal displacement, the acquired deformation patterns from these two tracks may look quite different. This is because the radar-imaging geometries of these two datasets are different. Therefore, we assume that landslides mainly occur in those portions of the study area with a slope larger than 10° (e.g., Zhao et al., 2012) and no obvious horizontal deformation in the flat regions (the region with a slope angle smaller than 10°). Given that the incidence angles of the InSAR measurements from the ascending and descending tracks are similar in the study area, the difference of linear deformation rate in the flat regions were used to form the two histograms. As shown in the figure, both distributions of the deformation difference from SP and NSP are similar to a normal distribution (mean of zero). The standard deviation of the deformation difference from SP and NSP is 1.2 cm/year and 1.7 cm/year, respectively. We should note that even if the landslide prone areas were masked, the deformation difference induced by the east-west deformation still cannot be ruled out completely. Therefore, the standard deviation of the deformation difference is only used as a relative comparison between the SP and NSP. The standard deviation of the deformation difference from SP is about 29% lower than that from NSP.

The time-series deformation rates from the SP and NSP are finally obtained. Although a spatial-temporal filter was used to separate the residual atmospheric phase, some results from the NSP are still severely

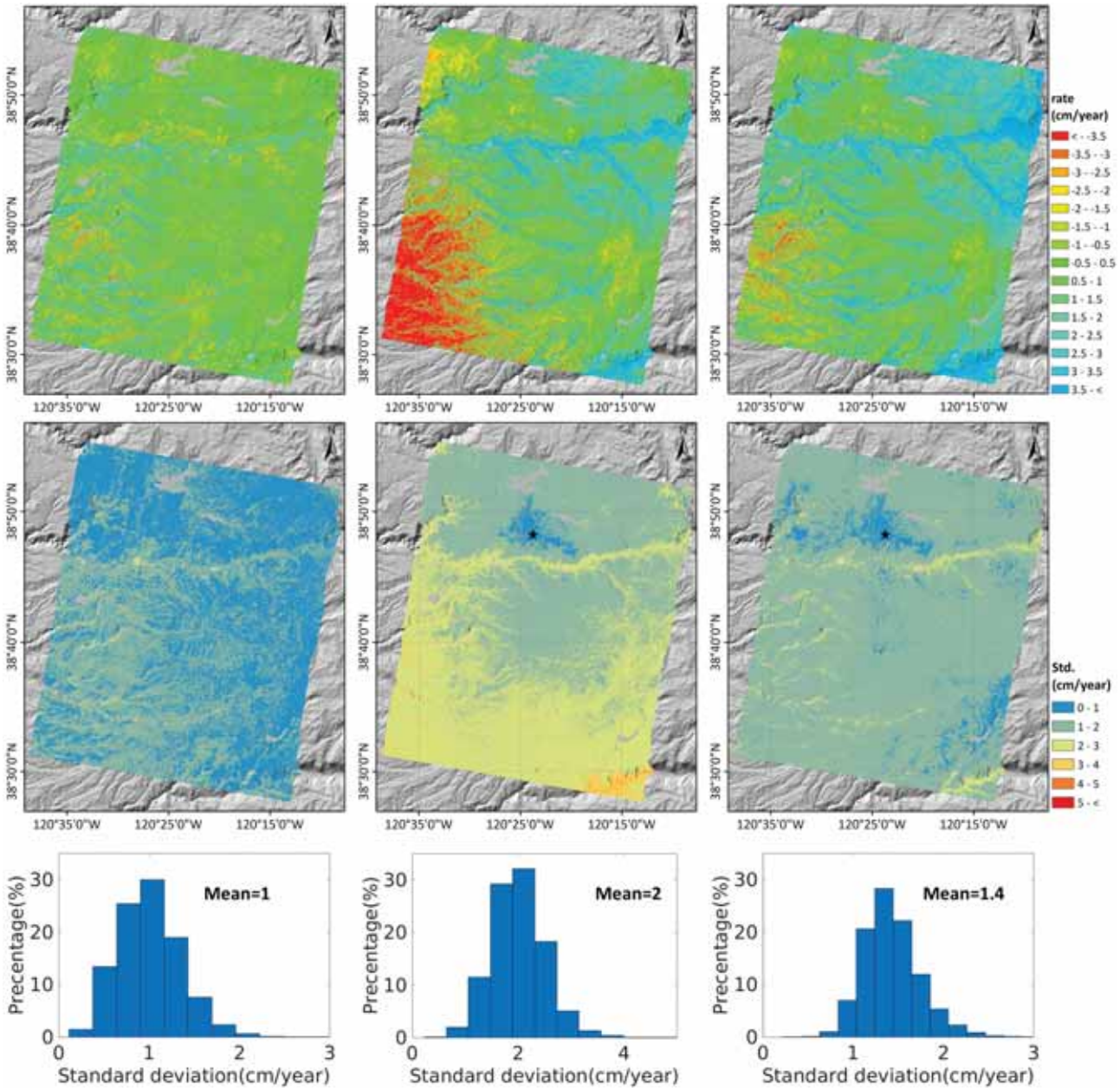

Fig. 7. A comparison of descending dataset results for linear deformation rate (top row), standard deviation of the deformation rate (second row) and histogram of the standard deviation (bottom row) for three processing methodologies: SP, NSPG, and NSP. The left column shows segment processing (SP) results; the center column shows non-segment processing with the GACOS correction (NSPG) results; the right column shows non-segment processing (NSP) results. The black star represents the reference point used for NSPG and NSP.

affected by atmospheric noise (as shown in the Supplementary Fig. S4). The magnitude and correlation distance of the spatial noise in the time series deformation from SP are obviously smaller than those of the NSP. In order to further compare and evaluate the time-series results, for simplicity, we assume that the structure of statistical properties of the residual atmospheric delay is spatially stationary. The 1-D covariance function (Wang et al., 2012), $\varepsilon = \sigma^2 e^{-k/\alpha}$, was used to model the spatial noise on time-series deformation rate, where ε is the covariance for the two pixels, σ^2 is the variance that indicates the variability of the results in spatial. This variance reflects the magnitude of spatial noise. α is the e-folding wavelength which shows the spatial correlated distance of the residual atmospheric delay. Regions with a linear deformation rate larger than 1 cm/year obtained by SP were masked to reduce the impact from the deformation signal of the unstable regions. Before covariance estimation, we interpolated the holes of each time series deformation rate spatially. As shown in Fig. 10, both the amplitude of the covariance and the spatial correlated distance using SP are smaller than those from NSP. For SP, the mean standard deviations (Fig. 10 insets, red σ) from ascending and descending track data are both about 0.11 mm/day. And for NSP, the mean standard deviation of the results from ascending and descending track are 0.15 mm/day and 0.13 mm/day, respectively (Fig. 10 insets, blue σ). In addition, the average e-folding wavelength from the SP and NSP are about 1 km and 5 km, respectively. These results show that, due to the individual processing in each segment, the spatial correlation distance and the magnitude of the atmospheric noise can be significantly reduced by SP compared with NSP.

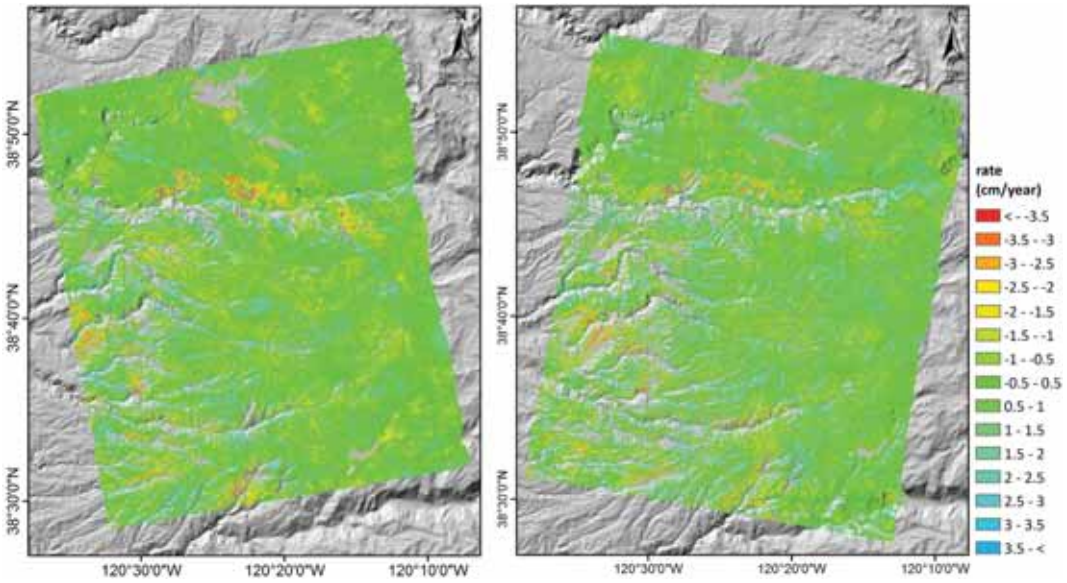

Fig. 8. Final linear deformation rate in line-of-sight (LOS) direction based on SP from the ascending track (left) and descending track (right).

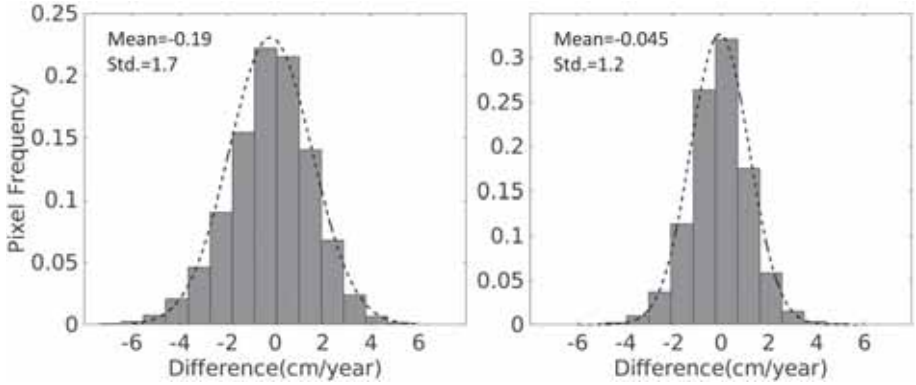

Fig. 9. Deformation rate difference between ascending and descending Sentinel-1 data using NSP results (left) and SP results (right).

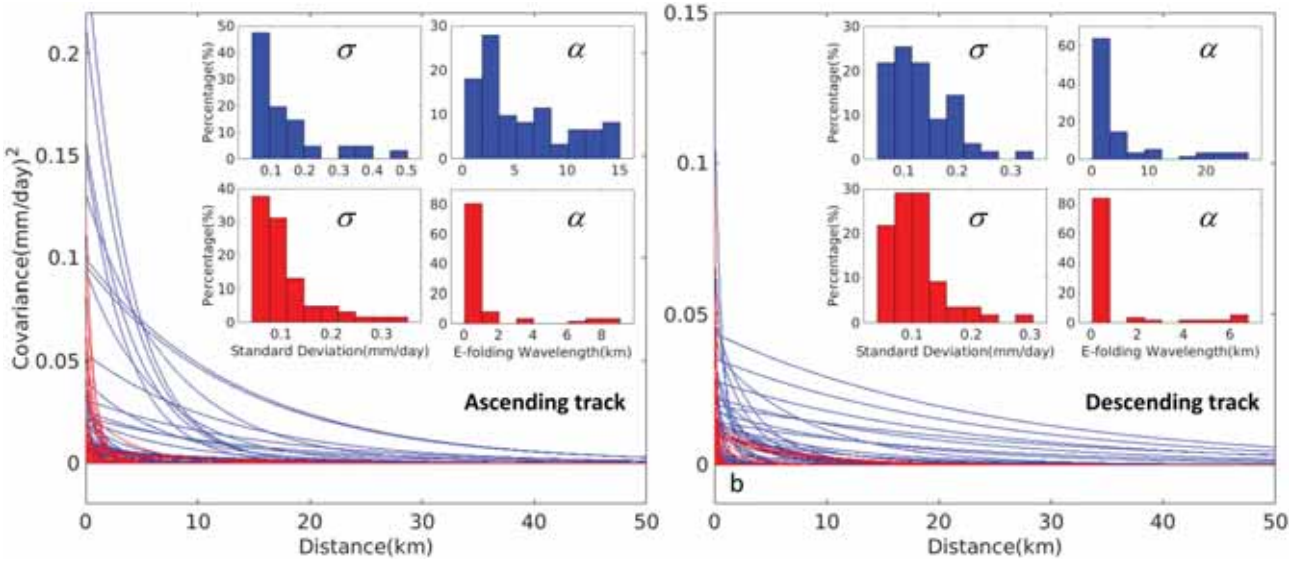

Fig. 10. Exponential covariance function of the time-series deformation rate from NSP (blue) and SP (red). Insets show distribution of the standard deviation and e-folding wavelength of the 1-D covariance function for the ascending track (left) and the descending track (right). (For interpretation of the references to colour in this figure legend, the reader is referred to the web version of this article.)

5.2. Landslide along the Highway 50 corridor

5.2.1. Spatial deformation rate

As shown in Fig. 11, obvious deformation signals along Highway 50 can be detected from both the ascending and descending datasets. Considering the corridor is a landslide-prone region (as shown in the Fig. 1), we suggest that these deformation signals mainly come from the creep of landslides. The acquired deformation is the projection of landslides' three-dimensional deformation on the line-of-sight direction (LOS) of radar. Negative values indicate landslide movement away from the satellite. We found that those landslides within the region S (dashed rectangle in Fig. 11a) show relatively larger deformation both in magnitude and scale, with maximum creeping rates from the ascending and descending track having reached about -7 ± 1 cm/year and -6 ± 1.1 cm/year in LOS directions, respectively. The uncertainty represents one standard deviation of the maximum deformation, indicating the variability of the results. Some traditional landslide identification methods delineate the landslides according to various surface characteristics (such as cracks, scarp and faults). However, some creep-stage landslides have no obvious surface characteristics, making them

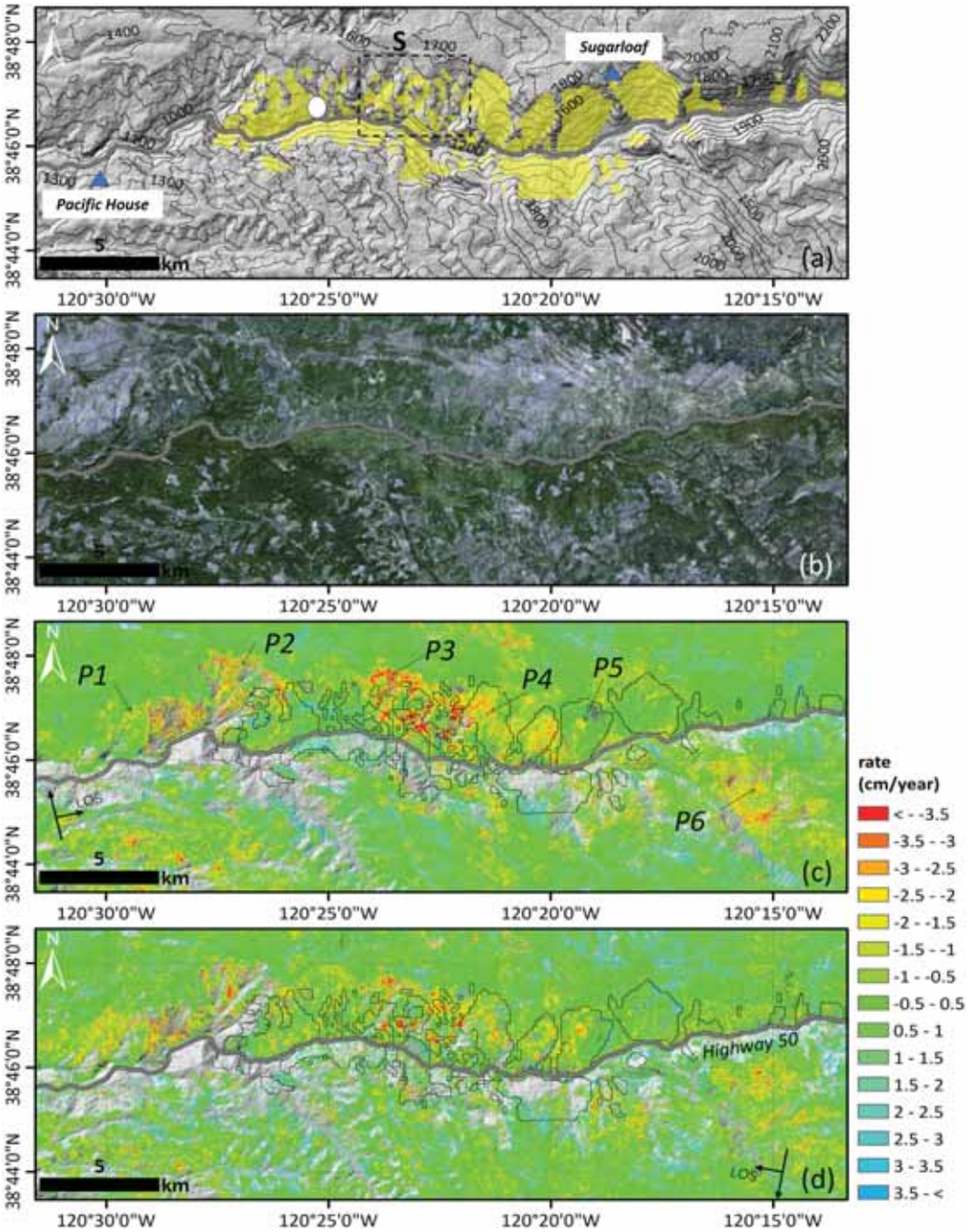

Fig. 11. (a) Terrain of the corridor along Highway 50. The yellow shading depicts documented landslides. The white ellipse shows the location of the Cleveland Corral landside, and the blue triangles represents the location of two weather stations; (b) A Sentinel-2 optical image obtained on September 12, 2019 through Copernicus open access hub provided by the European Space Agency (ESA)'s Copernicus Programme; (c) Linear deformation rate in LOS direction from ascending track, and the points P1-P6 are the selected locations for time-series analysis. The black lines outline the boundaries of the documented landslides; (d) Linear deformation rate in LOS direction from descending track. The black lines outline the boundaries of the documented landslides. (For interpretation of the references to colour in this figure legend, the reader is referred to the web version of this article.)

difficult to identify with traditional methods. Results obtained by this study may therefore provide new information for landslide inventory in this region. We also found that many results on the south side of Highway 50 were masked by setting the standard deviation threshold. We suggest that this is due to the interferogram decorrelation caused by vegetation. As shown in the Fig. 11, the regions where the deformation are masked are usually covered by dense vegetation.

Multi-track InSAR measurements can be used to derive the east-west and vertical components of deformation of landslides measured (e.g. Liu et al., 2020; Béjar-Pizarro et al., 2017). Since the SAR satellite orbits close to a north-south orientation, InSAR is more sensitive to the deformation in the vertical and the east-west directions than in the north-south direction (e.g. Wright et al., 2004; Samsonov and d'Oreye, 2012). Based on the SAR track angles and incidence angles at the center of our study site, the relationship between the three-dimensional ground deformation components and the InSAR measurements v_{los} acquired by our study can be expressed as follows,

$$\begin{bmatrix} v^a_{los} \\ v^d_{los} \end{bmatrix} = \begin{bmatrix} sin\theta^a sin\beta^a & -sin\theta^a cos\beta^a & cos\theta^a \\ sin\theta^d sin\beta^d & -sin\theta^d cos\beta^d & cos\theta^d \end{bmatrix} \begin{bmatrix} v_N \\ v_E \\ v_U \end{bmatrix} \tag{3}$$

where the superscripts a and d correspond to the ascending and descending track respectively, θ and β represent the incidence angle and the track angle respectively, and the v_N, v_E and v_U represent the north, east and vertical deformation components respectively.

For our datasets, the incidence angles (ascending: 39°, descending: 36°) and the track angles (ascending: −10°, descending: −167°) are introduced, the above equation becomes,

$$\begin{bmatrix} v^a_{los} \\ v^d_{los} \end{bmatrix} = \begin{bmatrix} -0.14 & -0.61 & 0.78 \\ -0.13 & 0.57 & 0.81 \end{bmatrix} \begin{bmatrix} v_N \\ v_E \\ v_U \end{bmatrix} \tag{4}$$

We can see the sensitivity of the motion in north-south direction much less than those in other directions. Therefore, in the 2-D deformation decomposition, the contribution in the north-south direction can be ignored when the deformation in the north-south direction is not significantly larger than that in the east-west and vertical directions (Samsonov and d'Oreye, 2012; Liu et al., 2020). However, considering the slope aspect of the corridor, the deformation of the landslides along the Highway 50 corridor mainly occur in north-south direction. This indicates that we cannot accurately decompose the vertical and east-west deformations for these landslides based on the results with ascending and descending tracks by ignoring the deformation in the north-south direction. In addition, in many cases the InSAR measurements of landslides can be decomposed or projected into other directions, given some assumptions. Usually, some prior information is needed for the assumptions. For example, some studies have decomposed or projected the deformation into 3-D or downslope directions by assuming that the landslide's basal plane was parallel to the ground surface (e.g. Ao et al., 2019; Hu et al., 2018; Kang et al., 2017; Zhao et al., 2012), which is suitable for the translational landslide. However, we don't know the specific types of all these landslides in this region. And the incidence angles from these descending and ascending observations are similar in the study area, which can cause unreliable decomposed deformation components of the landslides with north-south aspect angles (e.g. Hu et al., 2018). Therefore, the movements of these landslides were not decomposed or projected into other directions as part of this study.

5.2.2. Time-series deformation rate

We selected six monitoring points from different landslides for time-series analysis (Fig. 11c, points P1-P6). For each monitoring point, the linear deformation rates in LOS direction obtained from the ascending and descending datasets were similar. In order to further reduce the decorrelation noise, the average of time-series deformation rates (within in a 90 m wide square window) around the monitoring points were used for analysis. The standard deviations of the deformation rates around the monitoring points were set as an indicator of motion heterogeneity. As shown in Fig. 12, the time-series deformation rates from the ascending dataset (red) and the descending dataset (blue) agree quite well with each other. This phenomenon shows the reliability of the inverted time-series deformation.

All of these six points exhibit obvious seasonal deformation. For landslides, seasonal deformation is usually caused by seasonal precipitation, which can increase the pore-water pressure and reduce the Coulomb frictional strength of the landslide (Hu et al., 2019; Handwerger et al., 2016). The impact of pore-water pressure on a given landslide is related to precipitation, depth of the basal plane, hydraulic conductivity and diffusivity (Xu et al., 2019; Hu et al., 2019). So, different landslides always have different responses to precipitation (e.g. Zhao et al., 2012; Kang et al., 2019; Hu et al., 2018; Iverson, 2000; Hilley et al., 2004; Zhao et al., 2018).

Since the results are discontinuous in winter and early spring due to the low coherence, we assume that the creeping behaviors of these landslides continue during the periods of no InSAR measurements. From Fig. 12, it can be derived that these six landslides usually begin to accelerate from January to April of each year and peak in the dry season (May to October). The lag time between the peak of the deformation rate and the peak of precipitation (generally from January to April) are different, and at some monitoring points these lag times can be as long as several months. In addition, we have found that some landslides are more sensitive to cumulative precipitation in the rainy season rather than one heavy precipitation event. For example, the deformation rate of points P1, P2 and P3 are larger in 2017 and 2019 than in 2018, and the total precipitation of the rainy season from 2017 to 2018 was relatively lower than that of the adjacent rainy seasons.

The Cleveland Corral landside (location shown in Fig. 11a) is active in some wet years and has produced decimeter-level or meter-level movements in just a few months. The movements of this landslide are driven by pore-water pressure (Reid et al., 2003). However, in this study, the size of the Cleveland Corral landslide (width of ~25–70 m) is too small for InSAR to capture the deformation signal during the monitoring period. On this landslide site, the main form of precipitation is rainfall (Reid and Brien, 2019; Reid et al., 2003), and a cold weather storm could bring modest snowfall that usually melts within several days (Reid and Brien, 2019). The United States Geological Survey (USGS) has carried out real-time monitoring on this landslide since 1997, including precipitation, pore-water pressure and displacement. The thickness of this landslide ranges from 5 to 10 m (Reid et al., 2003; Aryal et al., 2015). According to the balanced cross-section method and the elastic dislocation model, the estimated maximum and average depth of the toe area of this landslide is about 6 m and 2.8 m respectively, similar to the observed slip depths of 2.37 m and 3.18 m (Aryal et al., 2015). The USGS released the monitoring report of the Cleveland Corral landslide from 1997 to 2013 (https://www.usgs.gov/natural-hazards/). We selected a period when this landslide was relative active, from October 2002 to October 2006, to analyze the dynamics of this landslide. From the yearly monitoring report of this landslide (the digitized results of which are shown in Fig. 13), we found that the pore-water pressure also exhibits a periodic fluctuation and that there is a time delay between pore-water pressure and precipitation. Although the precipitation usually increases beginning in November, the pore-water pressure, as measured from the deep sensor located about 3.69 m underground, often does not increase until January or February. In general, during the period of March to June, the pore-water pressure from the deep sensor can reach and maintain relatively high values for a period of time before the pore-water pressure decreases. During particularly wet years, rapid movement may occur after the pore pressure peaked in the late winter and early spring, as recorded by the deep sensor (Fig. 13).

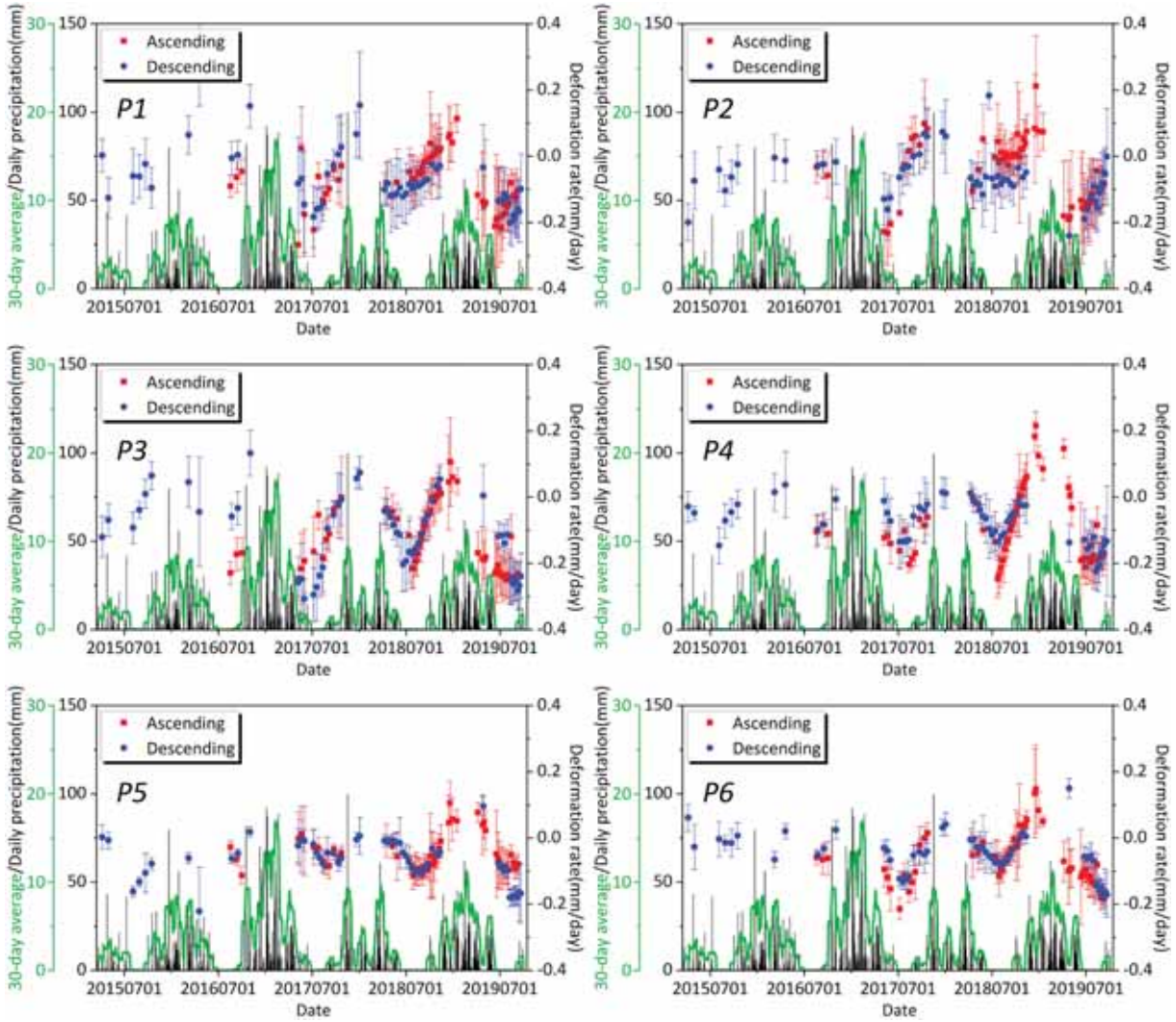

Fig. 12. The time-series deformation rates in LOS direction for the points P1 to P6, the location of these points is shown in Fig. 11 (c). The daily precipitation is collected from the Sugarloaf weather station (as shown in Fig. 11 (a)). Compared with the Pacific House weather station, the average distance between the Sugarloaf weather station and these six monitoring points is shorter.

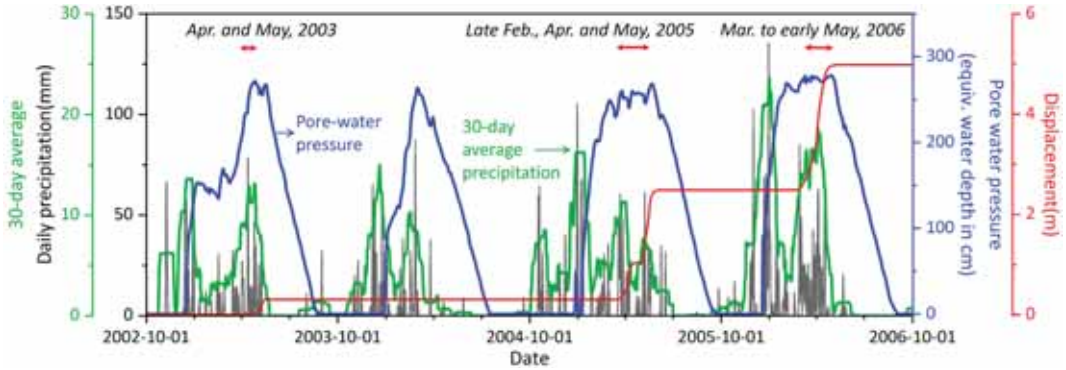

Fig. 13. The precipitation and the pore-water pressure from the deep sensor (about 3.69 m) of the Cleveland Corral landside. The daily precipitation data were collected from the Pacific House weather station, which is about 5 km from the Cleveland Corral landside. The location of the landslide and the station are shown in Fig. 11a. The pore-water pressure and the cumulative displacement were digitized from the USGS monitoring website (https://www.usgs.gov/natural-hazards/landslide-hazards/science). The red line represents the cumulative displacement, and its reference time is October 1st, 2002. (For interpretation of the references to colour in this figure legend, the reader is referred to the web version of this article.)

5.2.3. Pore-water pressure modeling

Based on the monitoring data of the Cleveland Corral landslide, we suggest that the periodic deformation of other landslides in this region may be also driven by pore-water pressure. And the pore-water pressure of the basal sliding surfaces needs some time to respond to the precipitation. In this study, a homogenous 1D diffusion model is used to simulate the changes of pore-water pressure at the subsurface and to explain the seasonal deformation of the landslide along the Highway 50 corridor (Hu et al., 2019; Handwerger et al., 2019).

$$\frac{dp}{dt} = D\frac{d^2p}{dz^2} \tag{5}$$

In which D represents the effective hydraulic diffusivity, p represents the pore-water pressure, z represents the underground depth, and t represents the time. The pore-water pressure at the ground surface is as follows,

$$p(t, z = 0) = q{\cdot}W(t) \tag{6}$$

where $W(t)$ is the precipitation which can be collected from the weather station, and q is a scaling factor, which controls the amplitude of pore-water pressure changes. Then, the solution of Eq. (6) is given as (Handwerger et al., 2019),

$$P(t, z) = \frac{z}{2\sqrt{\pi D}}\int_0^t \frac{e^{\frac{-z^2}{4D(t-m)}}}{\sqrt{(t-m)^3}}p(m, z = 0)dm \tag{7}$$

in which m is a variable of integration, the Eq. (7) can be solved in the Fourier domain, $\mathcal{F}$ and $\mathcal{F}^{-1}$ denotes the Fourier transform and the inverse Fourier transform respectively. The above equation in essence is a convolution of two functions $h(t)$ and $p(t, z = 0)$:

$$h(t) = \frac{z}{2\sqrt{\pi D t^3}}e^{\frac{-z^2}{4Dt}} \tag{8}$$

$$H(f) \sim \mathcal{F}[h(t)] \tag{9}$$

$$P(f, z = 0) \sim \mathcal{F}[p(t, z = 0)] \tag{10}$$

$$p(t, z) \sim \mathcal{F}^{-1}[H(f){\cdot}P(f, z = 0)] \tag{11}$$

Although this 1D diffusion model is relatively simple compared to some more complex models (Leshchinsky et al., 2019; Krzeminska et al., 2013), in landslide studies, this model has been widely applied to characterize the changes of precipitation-induced pore-water pressure (Iverson, 2000; Hu et al., 2019; Handwerger et al., 2019; Handwerger et al., 2016; Reid, 1994). In addition, it has been found that this model adequately describes the pore-water pressure changes for the Cleveland Corral landslide (Handwerger et al., 2016, in the supporting materials). Therefore, using the average precipitation from 1997 to 2013, we modeled the transient pore-water pressure within one calendar year. Based on the observation of the pore-water pressure at the depth of 3.69 m, the optimal effective hydraulic diffusivity can be determined. Then, the estimated effective hydraulic diffusivity was used to simulate the pore-water pressure at the depth of 10 m, and all the pore-water pressures were normalized respectively. At this location, the estimated effective hydraulic diffusivity is about 5×10^{-6} m^2/s, which is in the range of the effective hydraulic diffusivities of some other landslides in California (10^{-6} m^2/s to 10^{-4} m^2/s) (e.g., Iverson and Major, 1987; Cohen-Waeber et al., 2018; Hu et al., 2019; Handwerger et al., 2019).

As shown in Fig. 14, the 1D diffusion model can reflect the change of the pore-water pressure to some extent. Since the pore-water pressures are normalized separately, the simulated results only show the changes of pore-water pressure at different depths. At the depth of 3.69 m, the pore-water pressure reaches its peak in May. Therefore, if nearby landslides with a depth of 10 m have an effective hydraulic diffusivity similar to the Cleveland Corral landslide, the peak of the transient pore-water pressure of the basal plane will occur in July. While for the Cleveland Coral landslide, modest snowfall usually melts within several days (Reid and Brien, 2019), in winter and early spring, deep snowpack may exist in some regions of the Highway 50 corridor, and the resulting rapid snow melting in the spring is also considered a trigger for some landslides (Spittler and Wagner, 1998; Wagner and Spittler, 1997). This is because the water generated by snow melting will also infiltrate into the landslide and increase pore-water pressure. Thus, we can deduce that if the deep-seated landslides along Highway 50 have similar composition materials (particularly, clay rich) to the Cleveland Corral landslide, the deformation of these landslides in this region may peak in the summer (dry season). This phenomenon has a good correspondence with the InSAR observations under the assumption that the creep of these landslides is a continuous physical process (as shown in Fig. 12). Based on the above analysis, we suggest that the increase and decrease of pore-water pressure of the basal plane drive the periodic deformation of these landslides every year, and the peak deformation of the deep-seated landslides may occur at the dry season (May to October) in this region.

Finally, we have observed subtle upward movement of the landslides during the peak of the precipitation season (Fig. 12). Even though the deformation measurements during winter and early spring have large uncertainties due to relatively lower InSAR coherence, a consistent uplift signal can be found at most of the monitoring points in different years (Fig. 12). The upward movement of the landslide after the precipitation begins is likely due to an increase in the pore pressure of the landslide. More specifically, when the seasonal precipitation begins, the landslide becomes saturated due to infiltration and the pore-pressure

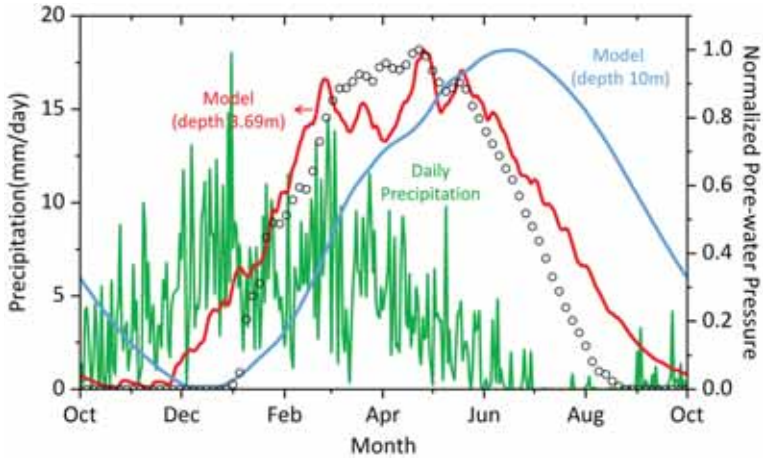

Fig. 14. The normalized transient pore-water pressure over one calendar year, superimposed on the average daily precipitation (from October 1997 to October 2013). The daily precipitation data were collected from the Pacific House weather station, which is about 5 km from the Cleveland Corral landside. The black circles represent the median values of the observed pore-water pressure at a depth of about 3.69 m. The red and blue lines represent the simulated pore-water pressures at 3.69 m and 10 m, respectively, based on the daily precipitation. (For interpretation of the references to colour in this figure legend, the reader is referred to the web version of this article.)

becomes large, causing the landslide to move up toward the satellite. The upward movement reaches a peak of 0.1 mm/day during the peak of precipitation. When the seasonal precipitation ends, then the water in the landslide drains away and the landslide subsides due to a reduction in the pressure. With continuing infiltration of the water into the basal plane, downslope movement of the landslide body is then superimposed to the subsidence of the landslide body, resulting in a larger apparent downward landslide movement. When the pore-water pressure reaches the base plane of ~10 m deep, a peak downward movement of 0.2 mm/day can be observed (Fig. 12). In other words, the downward deformation of the landslide is due to de-watering of the landslide body and downslope movement of the landslide along the basal plane while the upward deformation is due to increases in pore-pressures caused by infiltration. The fact that the upward and downward movement of the landslide are both very well correlated with the watering and de-watering that would occur in the landslide with seasonal precipitation also suggests the landslides contain clay-rich materials (Reid et al., 2003).

5.3. Other unstable regions

In addition to the landslides along the Highway 50 corridor, many other local unstable regions were also detected by radar satellites with ascending and descending tracks in the southwestern portion of the study area (Supplementary Fig. S7). Since the deformation is inverted in each segment individually, the peak of the long wavelength deformation signal may be left in the final result when the wavelength of the deformation signal is larger than the width of segment. However, from the results of the NSP and NSPG, the reliable long-wavelength deformation signal cannot be found in this area. The distribution of these local deformations is discrete, and many of these deformations can be found both in the ascending and descending datasets. So, we suggest that these deformations are mainly caused by some local instability. These deformation regions may contain some potential hazards that need to be further investigated and monitored.

6. Conclusion

In general, InSAR has the ability to map landslides with high precision and large coverage. However, in rural areas with large topographic fluctuations, InSAR results are severely affected by decorrelation noise and atmospheric artifacts. In order to reduce the impact of these errors, an interferogram selection method and a new InSAR SP technique are proposed and applied to the study area in the Eldorado National Forest. In SP, quadtree is used to divide interferograms based on height difference. Then, the phase-based APS correction, reference point selection and deformation inversion are performed in each segment individually. Finally, the results are merged and the residual atmospheric noise is separated by spatial-temporal filtering. In this study, SP shows an obvious advantage over NSP and NSPG for mapping local deformation; SP improved the average inner precision of the linear deformation rate by about 30% versus NSP. Moreover, the impact of the residual atmospheric noise on the time-series deformation from the SP was smaller than that from the NSP. However, it should be noted that SP is not suitable for regions with a long-wavelength deformation signal.

Possible spatial-temporal characteristics of the creeping deformation of multiple landslides along the Highway 50 corridor are revealed by this study. The 1D diffusion model was used to simulate the pore-water pressure and estimated the effective hydraulic diffusivity of the Cleveland Corral landslide. Based on the analysis of the precipitation, deformation and the pore-water pressure, we suggest that the seasonally time-series deformations of these landslides are driven by the pore-water pressure, and the peak of landslide movement can lag the peak of precipitation by a few months. In addition, we have observed transient upward deformation of the landslides due to expanding of the landslide body caused by pore-water pressure increases. These results provide new insights for the landslides along the Highway 50 corridor. Besides the known recorded landslides, some other local unstable regions were also detected by this study. These unstable regions may contain some potential landslide hazards that need further investigation and tracking. The methods presented in this study can be extended to other similar applications.

Declaration of Competing Interest

None.

Acknowledgments

We thank Xie Hu of UC Berkeley for providing helpful comments in the pore-water pressure modeling, Lei Zhang of the Hong Kong Polytechnic University for providing the interferogram segmentation program, David Annis from US Forest Service for providing helpful comments, Mark Reid from USGS for providing the depth of the pore water sensor, Colton Conroy for useful discussion on landslide deformation due to changes in pore-water pressure, and Associate Editor and two anonymous reviewers for constructive comments that improved the manuscript. The authors would like to thank the European Space Agency for providing the Sentinel-1A/B SAR data and Sentinel-2 optical image freely. One-arc-second SRTMDEM was freely downloaded from the website http://e4ftl01.cr.usgs.gov/MODV6_Dal_D/SRTM/. Global Precipitation Measurement (GPM) was freely downloaded from the website https://pmm.nasa.gov/data-access/downloads/gpm. The weather data was freely downloaded from the National Oceanic and Atmospheric Administration (https://www.noaa.gov/) and the Western Regional Climate Center (https://wrcc.dri.edu/). This research was funded by the US Forest Service (18-CR-11052007-072), the Fundamental Research Foundation of the Central Universities (No. 300102268704), the China Scholarship Council (No. 201806560020), and the Shuler-Foscue Endowment at Southern Methodist University.

Appendix A. Supplementary data

Supplementary data to this article can be found online at https://doi.org/10.1016/j.rse.2021.112400.

References

Albino, F., Biggs, J., Syahbana, D.K., 2019. Dyke intrusion between neighbouring arc volcanoes responsible for 2017 pre-eruptive seismic swarm at Agung. Nat. Commun. 10 (1), 1–11.

Ao, M., Zhang, L., Shi, X., Liao, M., Dong, J., 2019. Measurement of the three-dimensional surface deformation of the Jiaju landslide using a surface-parallel flow model. Remote Sensing Lett. 10 (8), 776–785.

Aryal, A., Brooks, B.A., Reid, M.E., Bawden, G.W., Pawlak, G.R., 2012. Displacement fields from point cloud data: application of particle imaging velocimetry to landslide geodesy. J. Geophys. Res. Earth Surf. 117 (F1).

Aryal, A., Brooks, B.A., Reid, M.E., 2015. Landslide subsurface slip geometry inferred from 3-D surface displacement fields. Geophys. Res. Lett. 42 (5), 1411–1417.

Bateson, L., Cigna, F., Boon, D., Sowter, A., 2015. The application of the intermittent SBAS (ISBAS) InSAR method to the South Wales coalfield, UK. Int. J. Appl. Earth Obs. Geoinf. 34, 249–257.

Béjar-Pizarro, M., Socquet, A., Armijo, R., Carrizo, D., Genrich, J., Simons, M., 2013. Andean structural control on interseismic coupling in the North Chile subduction zone. Nat. Geosci. 6, 462–467. https://doi.org/10.1038/NGEO1802.

Béjar-Pizarro, M., Notti, D., Mateos, R.M., Ezquerro, P., Centolanza, G., Herrera, G., Fernández, J., 2017. Mapping vulnerable urban areas affected by slow-moving landslides using Sentinel-1 InSAR data. Remote Sens. 9 (9), 876.

Bekaert, D.P.S., Hooper, A., Wright, T.J., 2015a. A spatially variable power law tropospheric correction technique for InSAR data. J. Geophys. Res. Solid Earth 120 (2), 1345–1356.

Bekaert, D.P.S., Walters, R.J., Wright, T.J., Hooper, A.J., Parker, D.J., 2015b. Statistical comparison of InSAR tropospheric correction techniques. Remote Sens. Environ. 170, 40–47.

Berardino, P., Fornaro, G., Lanari, R., Sansosti, E., 2002. A new algorithm for surface deformation monitoring based on small baseline differential SAR interferograms. IEEE Trans. Geosci. Remote Sens. 40 (11), 2375–2383.

Berube, N., 1999. Geologic Properties of the Cleveland Corral Landslide, Riverton, California. Master's Theses. San Jose State University.

Biggs, J., Wright, T., Lu, Z., Parsons, B., 2007. Multi-interferogram method for measuring interseismic deformation: Denali fault, Alaska. Geophys. J. Int. 170 (3), 1165–1179.
Cao, Y., Li, Z., Wei, J., Hu, J., Duan, M., Feng, G., 2018. Stochastic modeling for time series InSAR: with emphasis on atmospheric effects. J. Geod. 92 (2), 185–204.
Cigna, F., Sowter, A., 2017. The relationship between intermittent coherence and precision of ISBAS InSAR ground motion velocities: ERS-1/2 case studies in the UK. Remote Sens. Environ. 202, 177–198.
Cohen-Waeber, J., Bürgmann, R., Chaussard, E., Giannico, C., Ferretti, A., 2018. Spatiotemporal patterns of precipitation-modulated landslide deformation from independent component analysis of InSAR time series. Geophys. Res. Lett. 45 (4), 1878–1887.
Dong, J., Zhang, L., Liao, M., Gong, J., 2019. Improved correction of seasonal tropospheric delay in InSAR observations for landslide deformation monitoring. Remote Sens. Environ. 233, 111370.
Ferretti, A., Prati, C., Rocca, F., 2001. Permanent scatterers in SAR interferometry. IEEE Trans. Geosci. Remote Sens. 39 (1), 8–20.
Finnegan, N.J., Pritchard, M.E., Lohman, R.B., Lundgren, P.R., 2008. Constraints on surface deformation in the Seattle, WA, urban corridor from satellite radar interferometry time-series analysis. Geophys. J. Int. 174 (1), 29–41.
Gee, D., Sowter, A., Novellino, A., Marsh, S., Gluyas, J., 2016. Monitoring land motion due to natural gas extraction: validation of the intermittent SBAS (ISBAS) DInSAR algorithm over gas fields of North Holland, the Netherlands. Mar. Pet. Geol. 77, 1338–1354.
Gee, D., Bateson, L., Grebby, S., Novellino, A., Sowter, A., Wyatt, L., Athab, A., 2020. Modelling groundwater rebound in recently abandoned coalfields using DInSAR. Remote Sens. Environ. 249, 112021.
Handwerger, A.L., Rempel, A.W., Skarbek, R.M., Roering, J.J., Hilley, G.E., 2016. Rate-weakening friction characterizes both slow sliding and catastrophic failure of landslides. Proc. Natl. Acad. Sci. 113 (37), 10281–10286.
Handwerger, A.L., Huang, M.H., Fielding, E.J., Booth, A.M., Bürgmann, R., 2019. A shift from drought to extreme rainfall drives a stable landslide to catastrophic failure. Sci. Rep. 9 (1), 1–12.
Hilley, G.E., Bürgmann, R., Ferretti, A., Novali, F., Rocca, F., 2004. Dynamics of slow-moving landslides from permanent scatterer analysis. Science 304 (5679), 1952–1955.
Hong, Y., Adler, R., Huffman, G., 2006. Evaluation of the potential of NASA multi-satellite precipitation analysis in global landslide hazard assessment. Geophys. Res. Lett. 33 (22).
Hooper, A., Segall, P., Zebker, H., 2007. Persistent scatterer interferometric synthetic aperture radar for crustal deformation analysis, with application to Volcán Alcedo, Galápagos. J. Geophys. Res. Solid Earth 112 (B7).
Hooper, A., Bekaert, D., Spaans, K., Arıkan, M., 2012. Recent advances in SAR interferometry time series analysis for measuring crustal deformation. Tectonophysics 514, 1–13.
Hu, X., Bürgmann, R., 2020. Rheology of a Debris Slide from the Joint Analysis of UAVSAR and LiDAR Data. Geophys. Res. Lett. 47 (8) e2020GL087452.
Hu, X., Wang, T., Pierson, T.C., Lu, Z., Kim, J., Cecere, T.H., 2016. Detecting seasonal landslide movement within the Cascade landslide complex (Washington) using time-series SAR imagery. Remote Sens. Environ. 187, 49–61.
Hu, X., Lu, Z., Pierson, T.C., Kramer, R., George, D.L., 2018. Combining InSAR and GPS to determine transient movement and thickness of a seasonally active low-gradient translational landslide. Geophys. Res. Lett. 45 (3), 1453–1462.
Hu, X., Bürgmann, R., Lu, Z., Handwerger, A.L., Wang, T., Miao, R., 2019. Mobility, thickness, and hydraulic diffusivity of the slow-moving Monroe landslide in California revealed by L-band satellite radar interferometry. J. Geophys. Res. Solid Earth 124 (7), 7504–7518.
Huffman, G.J., Stocker, E.F., Bolvin, D.T., Nelkin, E.J., Tan, Jackson, 2019. GPM IMERG Final Precipitation L3 1 day 0.1 degree x 0.1 degree V06, Edited by Andrey Savtchenko, Greenbelt, MD, Goddard Earth Sciences Data and Information Services Center (GES DISC). Accessed: [Data Access Date]. https://doi.org/10.5067/GPM/IMERGDF/DAY/06.
Iverson, R.M., 2000. Landslide triggering by rain infiltration. Water Resour. Res. 36 (7), 1897–1910.
Iverson, R.M., Major, J.J., 1987. Rainfall, ground-water flow, and seasonal movement at Minor Creek landslide, northwestern California: physical interpretation of empirical relations. Geol. Soc. Am. Bull. 99 (4), 579–594.
Kang, Y., Zhao, C., Zhang, Q., Lu, Z., Li, B., 2017. Application of InSAR techniques to an analysis of the Guanling landslide. Remote Sens. 9 (10), 1046.
Kang, Y., Lu, Z., Zhao, C., Zhang, Q., Kim, J.W., Niu, Y., 2019. Diagnosis of Xinmo (China) landslide based on interferometric synthetic aperture radar observation and modeling. Remote Sens. 11 (16), 1846.
Kim, J.W., Lu, Z., 2018. Association between localized geohazards in West Texas and human activities, recognized by sentinel-1A/B satellite radar imagery. Sci. Rep. 8 (1), 4727.
Kim, J.W., Lu, Z., Kaufmann, J., 2019. Evolution of sinkholes over wink, Texas, observed by high-resolution optical and SAR imagery. Remote Sens. Environ. 222, 119–132.
Kruskal, J.B., 1956. On the shortest spanning subtree of a graph and the traveling salesman problem. Proc. Am. Math. Soc. 7 (1), 48–50.
Krzeminska, D.M., Bogaard, T.A., Malet, J.P., Van Beek, L.P.H., 2013. A model of hydrological and mechanical feedbacks of preferential fissure flow in a slow-moving landslide. Hydrol. Earth Syst. Sci. 17 (3).
Kwoun, O., Lu, Z., Neal, C., Wicks, C., 2006. Quiescent deformation of the Aniakchak caldera, Alaska, mapped by InSAR. Geology 34 (1), 5–8.
Lauknes, T.R., Zebker, H.A., Larsen, Y., 2010. InSAR deformation time-series using an L1-norm small-baseline approach. IEEE Trans. Geosci. Remote Sens. 49 (1), 536–546.
Lee, C.W., Lu, Z., Jung, H.S., Won, J.S., Dzurisin, D., 2010. Surface deformation of Augustine volcano, 1992–2005, from multiple-interferogram processing using a refined small baseline subset (SBAS) interferometric synthetic aperture radar (InSAR) approach. The 2006 eruption of Augustine Volcano, Alaska. U.S. Geological Survey Professional Paper. U.S. Geological Survey, pp. 453–465.
Leshchinsky, B., Olsen, M.J., Mohney, C., O'Banion, M., Bunn, M., Allan, J., McClung, R., 2019. Quantifying the sensitivity of progressive landslide movements to failure geometry, undercutting processes and hydrological changes. J. Geophys. Res. Earth Surf. 124 (2), 616–638.
Liang, H., Zhang, L., Ding, X., Lu, Z., Li, X., 2018. Toward mitigating stratified tropospheric delays in multitemporal InSAR: a quadtree aided joint model. IEEE Trans. Geosci. Remote Sens. 57 (1), 291–303.
Liu, X., Zhao, C., Zhang, Q., Yang, C., Zhu, W., 2020. Heifangtai loess landslide type and failure mode analysis with ascending and descending spot-mode TerraSAR-X datasets. Landslides 17 (1), 205–215.
Lohman, R.B., Simons, M., 2005. Some thoughts on the use of InSAR data to constrain models of surface deformation: noise structure and data downsampling. Geochem. Geophys. Geosyst. 6 (1).
Lu, Z., Dzurisin, D., 2014. InSAR Imaging of Aleutian Volcanoes: Monitoring a Volcanic Arc from Space. Springer Praxis Books, Geophysical Sciences, p. 390. ISBN 978-3-642-00347-9.
Lu, Z., Kwoun, O., 2008. Radarsat-1 and ERS interferometric analysis over southeastern coastal Louisiana: implication for mapping water-level changes beneath swamp forests. IEEE Trans. Geosci. Remote Sens. 46, 2167–2184.
Lu, Z., Power, J., McConnell, V., Wicks, C., Dzurisin, D., 2002. Pre-Eruptive inflation and surface interferometric coherence characteristics revealed by satellite radar interferometry at Makushin volcano, Alaska: 1993–2000. J. Geophys. Res. 107 (B11), 2266. https://doi.org/10.1029/2001JB000970.
Morishita, Y., Lazecky, M., Wright, T.J., Weiss, J.R., Elliott, J.R., Hooper, A., 2020. LiCSBAS: an open-source InSAR time-series analysis package integrated with the LiCSAR automated Sentinel-1 InSAR processor. Remote Sens. 12 (3), 424.
Murray, K.D., Bekaert, D.P., Lohman, R.B., 2019. Tropospheric corrections for InSAR: statistical assessments and applications to the Central United States and Mexico. Remote Sens. Environ. 232, 111326.
Nikolaeva, E., Walter, T.R., Shirzaei, M., Zschau, J., 2014. Landslide observation and volume estimation in Central Georgia based on L-band InSAR. Nat. Hazards Earth Syst. Sci. (NHESS) 14 (3), 675–688.
Novellino, A., Cigna, F., Sowter, A., Ramondini, M., Calcaterra, D., 2017. Exploitation of the intermittent SBAS (ISBAS) algorithm with COSMO-SkyMed data for landslide inventory mapping in North-Western Sicily, Italy. Geomorphology 280, 153–166.
Parizzi, A., Brcic, R., De Zan, F., 2020. InSAR performance for large-scale deformation measurement. IEEE Trans. Geosci. Remote Sens. https://doi.org/10.1109/TGRS.2020.3039006.
Reid, M.E., 1994. A pore-pressure diffusion model for estimating landslide-inducing rainfall. J. Geol. 102 (6), 709–717.
Reid, M.E., Brien, D.L., 2019. Debris-flow initiation promoted by extension within a slow-moving landslide. In: Seventh International Conference on Debris-Flow Hazards Mitigation, pp. 824–831.
Reid, M.E., Brien, D.L., LaHusen, R.G., Roering, J.J., De La Fuente, J., Ellen, S.D., 2003. Debris-flow initiation from large, slow-moving landslides. In: Rickenmann, D., Chen, C.L. (Eds.), Debris-Flow Hazards Mitigation: Mechanics, Prediction, and Assessment, vol. 1, pp. 155–166.
Samsonov, S., d'Oreye, N., 2012. Multidimensional time-series analysis of ground deformation from multiple InSAR data sets applied to Virunga Volcanic Province. Geophys. J. Int. 191 (3), 1095–1108.
Sowter, A., Bateson, L., Strange, P., Ambrose, K., Syafiudin, M.F., 2013. DInSAR estimation of land motion using intermittent coherence with application to the south Derbyshire and Leicestershire coalfields. Remote Sensing Lett. 4 (10), 979–987.
Sowter, A., Amat, M.B.C., Cigna, F., Marsh, S., Athab, A., Alshammari, L., 2016. Mexico City land subsidence in 2014–2015 with Sentinel-1 IW TOPS: results using the intermittent SBAS (ISBAS) technique. Int. J. Appl. Earth Obs. Geoinf. 52, 230–242.
Spittler, T.E., Wagner, D.L., 1998. Geology and slope stability along highway 50. Calif. Geol. 51 (3), 3–14.
Wagner, D.L., Spittler, T.E., 1997. Landsliding along the Highway 50 Corridor: Geology and Slope Stability of the American River Canyon between Riverton and Strawberry. California Department of Conservation Division of Mines and Geology, California.
Wang, H., Wright, T.J., Yu, Y., Lin, H., Jiang, L., Li, C., Qiu, G., 2012. InSAR reveals coastal subsidence in the Pearl River Delta, China. Geophys. J. Int. 191 (3), 1119–1128.
Werner, C., Wegmüller, U., Strozzi, T., Wiesmann, A., 2000. GAMMA SAR and interferometric processing software. In: Proceedings of ERS - ENVISAT Symposium, Gothenburg, Sweden, 16-20 Oct. 2000.
Wright, T., Parsons, B., Lu, Z., 2004. Toward mapping surface deformation in three dimensions using InSAR. Geophys. Res. Lett. 31 https://doi.org/10.1029/2003GL018827. L01607.
Xu, B., Li, Z.W., Wang, Q.J., Jiang, M., Zhu, J.J., Ding, X.L., 2013. A refined strategy for removing composite errors of SAR interferogram. IEEE Geosci. Remote Sens. Lett. 11 (1), 143–147.
Xu, Y., Kim, J., George, D.L., Lu, Z., 2019. Characterizing seasonally rainfall-driven movement of a translational landslide using SAR imagery and SMAP soil moisture. Remote Sens. 11 (20), 2347.
Yu, C., Li, Z., Penna, N.T., Crippa, P., 2018. Generic atmospheric correction model for interferometric synthetic aperture radar observations. J. Geophys. Res. Solid Earth 123 (10), 9202–9222.
Zebker, H.A., Villasenor, J., 1992. Decorrelation in interferometric radar echoes. IEEE Trans. Geosci. Remote Sens. 30 (5), 950–959.

Zhao, C., Lu, Z., Zhang, Q., de La Fuente, J., 2012. Large-area landslide detection and monitoring with ALOS/PALSAR imagery data over northern California and southern Oregon, USA. Remote Sens. Environ. 124, 348–359.

Zhao, C., Kang, Y., Zhang, Q., Lu, Z., Li, B., 2018. Landslide identification and monitoring along the Jinsha River catchment (Wudongde reservoir area), China, using the InSAR method. Remote Sens. 10 (7), 993.

Zheng, W., Kim, J.W., Ali, S.T., Lu, Z., 2019. Wastewater leakage in West Texas revealed by satellite radar imagery and numerical modeling. Sci. Rep. 9 (1), 1–11.